Multi-tier mechanics control stromal adaptations in swelling lymph nodes

Frank P. Assen[1,2,*], Miroslav Hons[1,3], Robert Hauschild[1], Shayan Shamipour[1], Jun Abe[4], Walter A. Kaufmann[1], Tommaso Costanzo[1], Gabriel Krens[1], Markus Brown[1], Burkhard Ludewig[5], Simon Hippenmeyer[1], Jens V. Stein[4], Carl-Philipp Heisenberg[1], Edouard Hannezo[1], Sanjiv A. Luther[6], Michael Sixt[1,*]

[1]Institute of Science and Technology Austria (IST Austria), Klosterneuburg, Austria

[2]Department of Dermatology, Medical University Vienna, Vienna, Austria

[3]BIOCEV, First Faculty of Medicine, Charles University, Vestec, Czech Republic

[4]Department of Oncology, Microbiology and Immunology, University of Fribourg, Fribourg, Switzerland

[5]Institute of Immunobiology, Kantonsspital St Gallen, St Gallen, Switzerland

[6]Department of Biochemistry, University of Lausanne, Epalinges, Switzerland

[*]Correspondence to: Sixt@ist.ac.at; frank.assen@meduniwien.ac.at

Abstract

Lymph nodes (LNs) comprise two main structural elements: Fibroblastic reticular cells (FRCs) that form dedicated niches for immune cell interaction and capsular fibroblasts that build a shell around the organ. While LNs are fairly stable in size during homeostatic conditions, immunological challenge causes more than 10-fold increase in size within only a few days. How a solid organ can accommodate such extreme volumetric changes is poorly understood. Here, we characterize the biomechanics of LN swelling on the cellular and organ scale. We identify lymphocyte trapping by influx and proliferation as drivers of an outward pressure force, causing FRCs and their associated conduits to stretch. After an initial phase of relaxation, FRCs sense the resulting strain via cell matrix adhesions, which coordinates local growth and remodeling of the stromal network. While the expanded FRC network adopts its typical configuration, a massive fibrotic reaction of the organ capsule sets in and counters further organ expansion. Thus, different fibroblast populations mechanically control LN swelling in a multi-tier fashion.

Introduction

Lymph nodes (LNs) are the macroscopic organs of the adaptive immune system. As opposed to other organs, the LN parenchyma only contains few resident cells, while the bulk of lymphocytes is in transit. Lymphocytes circulate through the bodies' vascular systems, and from there they enter LNs via high endothelial venules (HEVs). Within the LN parenchyma, lymphocytes actively migrate to scan large numbers of potentially antigen-bearing dendritic cells (DCs). After several hours of unsuccessful search, lymphocytes exit the organ again via efferent lymphatic vessels that eventually drain back into the blood circulation and the cycle starts again[1,2]. Lymphocytes are densely packed within LNs and make up about 95% of its total cellularity. Despite dynamic cellular exchange, homeostatic LN size remains relatively stable. Known modulators of homeostatic LN cellularity (e.g., during circadian rhythms[3,4]) are mainly chemoattractants and adhesion molecules[2,5–8], which serve as entry and exit signals for lymphocytes, as well as stromal cell-derived survival factors[9–12] and adrenergic signals[13,14]. The main stromal cells found in LNs are FRCs. These form the non-hematopoietic backbone of the organ and deposit bundled fibers of extracellular matrix (ECM) that assemble an intricate 3D network termed conduits. FRCs enwrap these ECM conduits and form an interface with the immune cells[15,16]. They provide a multitude of signals that serve to compartmentalize the organ and support migration, cellular interactions and expansion of immune cell subsets[17–19].

Upon immunological challenge, reactive LNs swell rapidly by recruiting large numbers of naïve lymphocytes via HEVs, while lymphocyte egress via efferent lymphatics is initially blocked[20,21]. LNs can swell up to 10-fold in size in the order of days, imposing an internal structural problem on the FRC network that has to cope with this volumetric challenge. It has been demonstrated that FRCs are able to relax and expand upon interaction with activated DCs[22,23]. This has been proposed as one mechanism that allows the LN to create additional space during the swelling phase. In addition, FRC numbers expand during inflammation and various redundant mechanisms that drive this expansion in the early and late phase of LN swelling have been described[20,22–26]. The ratio of FRC- to lymphocyte numbers remains fairly constant in the swelling LN and trapping of naïve lymphocytes in the absence of inflammatory stimuli has been demonstrated as a sufficient stimulus for the FRC network to expand[20]. How network expansion is coordinated to prevent under- or overgrowth of the FRC network is unknown,

and although mechanical forces are obvious feedback parameters, these aspects of LN swelling have not been measured until to date.

We measure the cellular and mechanical changes accompanying LN swelling and show that mechanical load on the conduit network and subsequent FRC mechanosensing are central to expansion of the FRC network and LN growth.

69 ## Results

70 **The reactive lymph node resists swelling**

71 To understand the global mechanical behavior of LNs while expanding, we started out with a
72 quantitative characterization of bulk tissue properties of the reactive organ. Upon
73 immunization with keyhole limpet hemocyanin in complete Freund's adjuvant (KLH/CFA) in
74 footpads of wild-type (wt) mice, we observed a more than 10-fold increase in volume of
75 draining popliteal LNs after 14 days, when the organ reached its maximum size. The volume
76 was calculated from 2D side-view images, which correlated well with the weight of the organ
77 and showed that LNs swell on average about 0.75 mm^3 per day (Figure 1A,B & Figure S1A,B).
78 We measured tissue mechanics by compressing explanted popliteal LNs between two parallel
79 plates at 75% of their original height (25% strain), while the resisting force exerted by the LN
80 on the top plate was measured over a time period of 20-60 minutes (Figure 1C). During this
81 time the LN underwent a viscoelastic relaxation behavior and reached a new force-
82 equilibrium, which is described by the stress-relaxation curve (Figure 1D & Figure S1C,D).
83 Together with the geometrical parameters of LNs measured before compression and at the
84 new force-equilibrium, the *effective resistance* (σ, *surface tension*), the *viscosity* (μ_2, fluidic
85 resistance to deformation by an applied force), and the *elastic modulus* (Young's Modulus, or
86 elastic resistance to deformation by an applied force) of the tissue were derived by modelling
87 the parameters to a generalized Kelvin model (Figure S1E)[27]. At equilibrium (long time scale),
88 the LN resisted the external force exerted by the plate, which sets the *effective resistance*
89 (given in Newton/m). This parameter describes the collective forces resisting organ expansion
90 and is a measure of how much force is necessary to drive the swelling of the LN by a certain
91 length scale.

92 During the course of organ expansion (D0-D14), we observed a ~4-fold increase of effective
93 resistance and values remained elevated until the endpoint at D14 (Figure 1E). Viscosity – the
94 resistance to deformation on the medium time scale – only increased in the last phase of
95 swelling, while elasticity – the resistance to deformation on the short time scale – was
96 selectively increased from the homeostatic condition at D2 and D14 of inflammation (Figure
97 1F,G).

98 These data demonstrate that tissue properties of LNs show complex adaptive dynamics upon
99 swelling, and suggest that the mechanical features of the organ resist the forces driving
100 expansion.
101
102 **Lymphocyte numbers generate pressure and drive lymph node swelling**
103 Having defined that mechanical properties of the LN resist swelling, we next asked what are
104 the internal forces driving organ expansion. Lymphocytes constantly recirculate through LNs
105 where they are densely packed within the FRC scaffold (Figure S1F). Entry via HEVs, blocking
106 of exit in the early inflammation phase, and proliferation upon activation are the main factors
107 that increase cellularity of the node, making these potential factors driving expansion[28–30].
108 Hence, we manipulated entry and activation and tested the impact on LN bulk tissue
109 properties.
110 We first perturbed lymphocyte entry under homeostatic conditions using an L-selecting
111 antagonizing antibody; anti-CD62L (α-CD62L). L-selectin is expressed on naïve lymphocytes
112 and rate-limiting for transmigration via HEVs[31]. After 24h of either α-CD62L or PBS
113 intravenous (i.v.) injection, popliteal LNs from wt mice were harvested and used for parallel
114 plate compression experiments. We found that blocking of lymphocyte entry significantly
115 reduced LN volume, effective resistance and viscosity, while the Young's Modulus remained
116 unchanged (Figure 2A-E). These data suggest that lymphocyte influx represents an internal
117 force, balancing the effective resistance of the homeostatic LN.
118 Next, we asked how lymphocyte cellularity affects bulk tissue properties of LNs during
119 inflammatory swelling. In order to distinguish between contribution of recirculating and
120 locally proliferating lymphocytes, we treated wt or OT-II mice with either α-CD62L or PBS,
121 immunized with KLH/CFA and measured tissue properties after four days (Figure 2F-J). Mice
122 carrying the OT-II TCR transgene suppress their natural TCRs [31], thereby creating a situation
123 where lymphocyte homing is maintained but the majority of B and T cell responses against
124 the mismatched KLH antigen eliminated. Homing, and to a lesser extent proliferation,
125 contributed significantly to LN swelling, while elimination of both parameters reduced LN
126 volumes even further (Figure 2G). In agreement with the findings under homeostatic
127 conditions, α-CD62L administration reduced the effective resistance in both wt and OT-II
128 mice, with blockade of homing showing the dominant effect (Figure 2H). While the viscosity

129 in the tested conditions did not show a clear trend with lymphocyte cellularity, the Young's
130 Modulus was reduced when lymphocyte trafficking was blocked in inflammation (Figure 2I,J).
131 Thus, lymphocyte trapping is not a consequence of LN swelling but drives the process as it
132 generates an outward pressure force which is countered by the organ's effective resistance.
133

134 **The FRC network stretches upon lymph node swelling**

135 Next, we investigated which mechanical features of the LN are resisting it's expansion. The
136 two candidate structures mediating the LNs effective resistance to swelling are the organ
137 capsule, and the FRC- and conduit network. To understand how the FRC network adapts to
138 volumetric changes upon swelling we quantified FRC spacing (gaps) within the T zone over
139 the time course of inflammation in Ccl19-Cre*;* mTmG (FRC-mGFP) (membrane Tomato,
140 membrane Green Fluorescent Protein (GFP)) mice that selectively express membrane GFP
141 (mGFP) in FRCs[32,33]. To this end, a circle-fitting algorithm was used to quantify the distribution
142 of gaps in FRC networks from two-dimensional (2D) tissue sections (Figure 3A,B). While we
143 found no obvious disruptions of network integrity, the FRC network dynamically adapted over
144 time. In the first four days of inflammation the FRC network widened, as indicated by larger
145 gaps, and in the following days returned to homeostatic levels (Figure 3C,D).
146 These results suggest that the intact FRC network initially stretches upon swelling and
147 subsequently remodels to accommodate the increased numbers of proliferating and
148 immigrating lymphocytes.
149

150 **Conduits are stretched in the swelling lymph node**

151 The FRC network comprises two principal structural components: the FRC itself and the ECM
152 conduit, a complex fibrillar structure, which the myofibroblastic FRC both produces and
153 ensheathes (Figure 4A). Both components have the potential to bear load and confer
154 mechanical resistance to swelling. In the following, we devised strategies to quantitatively
155 measure if and to what extent the two structures experience mechanical forces. We started
156 out with the ECM component and as a proxy for mechanical strain, we chose to investigate
157 the structural organization of the conduit's fibrillar collagen. Like in tendons and other elastic
158 ECM structures, fibrillar alignment should increase with strain.
159 We fixed homeostatic and reactive LNs and removed all cellular components by alkali-
160 maceration (Figure S2A,B). To resolve the 3-dimensional (3D) organization of individual

161 collagen fibrils, scanning transmission electron microscopy (STEM) tomograms of T zone
162 conduits were acquired at 2 degrees differential tilting angles (Figure 4A). 3D images were
163 reconstructed using computed weight back projection (Figure S2C,D). We quantified the
164 extent of conduit stretching by 3D manual tracking of individual collagen fibril segments and
165 by computationally calculating the centerline of each conduit based on the average direction
166 of its collagen fibrils. This allowed us to determine the angle of misalignment of individual
167 fibril segments relative to the centerline (Figure 4C,D). We found that compared to
168 homeostasis (D0), early in inflammation (D2, D4) conduit collagen fibrils become
169 progressively aligned, whereas later in inflammation (D14) they again adopted a misaligned
170 configuration (Figure 4D).
171 These results suggest that conduits stretch and bear an increased mechanical load early upon
172 LN swelling. At later time points they revert to the homeostatic state. Initial stretching and
173 later adaptation are well in line with our previous findings on network configuration.
174
175 **FRC network tension increases upon lymph node swelling**
176 We next addressed the cellular component of the FRC stretching-response. To study if the
177 previously observed change in conduit conformation is mirrored by the tension-state of the
178 FRC network, we directly measured FRC network tension by intravital laser ablation and recoil
179 analysis[34,35]. To this end, inguinal LNs of FRC-mGFP mice were surgically exposed and the FRC
180 network was imaged around 20 µm below the capsule. Individual strands of the 3D network
181 were cut using a high-power ultra-violet (UV)-laser (Figure 5A). FRC network tension was
182 subsequently determined in kymographs by calculating local recoil velocities of the region
183 around the site of ablation (Figure 5B,C and Supplemental Movie 1). We found that at D4 and
184 D8 of inflammation the tension on the FRC network almost doubled and was restored again
185 to homeostatic levels at D14 of inflammation.
186 As a proxy for the cellular mechano-response, we next measured the nuclear vs. cytoplasmic
187 intensity of the transcription factors Yes-associated protein (YAP), and transcriptional co-
188 activator with PDZ binding motif (TAZ), which are well-established downstream responses of
189 cytoskeletal tension[36]. FRCs and endothelial cells stained positive for YAP/TAZ, while no signal
190 could be observed in leukocytes (Figure 5D,E). The nuclear:cytoplasmic ratio of YAP/TAZ (N:C
191 YAP/TAZ ratio) in FRCs remained stable from D0 to D2 of inflammation but increased at D4
192 and D8 of inflammation, confirming that FRCs experience increased cytoskeletal tension

193 during LN swelling. The N:C ratio decreased after FRC tension peaked (Figure 5C,F), thereby
194 faithfully recapitulating the tension as measured by laser cutting. Interestingly, after two
195 weeks of inflammation we observed a large population of FRCs that had a negative N:C ratio,
196 suggesting that those cells were completely shielded from active tension.
197 Together, these data demonstrate that FRC tension increases upon LN swelling. However,
198 compared with the ECM conduit (Figure 4), tension at the cellular level increases with a two
199 day time delay. This kinetic is well in line with previous observations, suggesting that early in
200 inflammation FRCs experience a relaxation of actomyosin contractility[22,23]. This relaxation is
201 transient and followed by an increase in cytoskeletal tension. At later time points when
202 network geometry adopts its homeostatic configuration, tension drops again.
203
204 **FRCs in the swelling lymph node undergo distributed clonal expansion**
205 The above data suggest that lymphocyte influx drives LN expansion, which initially stretches
206 the FRC network and elicits a mechanosensitive response by the cells, once their initial
207 relaxation[22,23] ceases. We next wanted to understand how the FRC network expands,
208 remodels and re-establishes its typical configuration and mechanical state, while maintaining
209 structural integrity.
210 To this end, we devised an approach to map the spatio-temporal expansion of the FRC
211 network in the swelling LN *in situ*. We used a sparse clonal labeling approach named Mosaic
212 Analysis with Double Markers (MADM)[37–39]. MADM labeling depends on rare
213 interchromosomal mitotic recombination driven by Cre-loxP sites (Figure S3A,B). Two
214 reciprocally split GFP and tdTomato genes (GT and TG) on identical loci of homologous
215 chromosomes are used to create transheterozygous offspring (GT/TG). Interchromosomal
216 recombination can take place in G_2 phase and restores functional GFP and tdTomato
217 expression. To trigger rare recombination specifically in FRCs we used the Ccl19-*Cre*
218 transgene[32]. When followed by X-segregation of chromosomes in mitosis, two daughter cells
219 are formed in which one expresses GFP (green lineage) and the other tdTomato (red lineage).
220 Recombination is irreversible and all subsequent progeny cells become part of the lineage.
221 Homeostatic and reactive LNs were cleared and imaged by 3D light-sheet fluorescence
222 microscopy (LSFM). In reactive nodes, prominent clusters of FRCs emerged at D4 and D8 of
223 inflammation, while such clusters were rarely observed in homeostasis (Figure 6A,B & Figure
224 S3C). This suggested that individual FRC clones expanded following immunization and that

225 daughter-FRCs stay close to their precursor. No substantial bias in red vs. green lineage was
226 apparent, justifying combined analyses (Figure S3D). FRC clusters were quantitatively
227 analyzed using a density-based spatial clustering of applications with noise (DBSCAN)[40] for
228 which FRC bodies were semi-automatically mapped in 3D as spheres with a 12 µm diameter
229 (Figure S3E). A cluster was defined as at least three FRCs from the same lineage within a radius
230 of 20 µm. We found that both the number of labeled FRCs, number of clusters and number
231 of FRCs in clusters were significantly increased in reactive nodes (Figure 6C-F). Since clusters
232 can arise by chance, the cluster results were compared to the average of 10 simulated
233 distributions in which the same number of FRCs were randomly distributed in the same
234 volume. Although clusters arise by chance in random distributions, FRCs in inflammation were
235 less uniformly distributed and formed more and larger clusters with FRC numbers ranging
236 from 3-14 (Figure 6G, Figure S3F). Clone size distribution was exponential as is expected from
237 an equipotent population of precursors that are dividing stochastically[41]. To quantify the
238 extent of FRC clustering within LNs, we defined a cluster factor (CF) as the ratio of the number
239 of FRCs found in clusters between the observed and simulated distributions (Figure S3G).
240 Hence, a CF of 100 indicates that 100x more cells are found in clusters as by chance alone.
241 We found an average CF of 5 in homeostatic conditions and 117 in inflammation (respectively,
242 70 and 165 for D4 and D8), confirming that FRCs form clusters in the swelling LN (Figure 6H).
243 We next investigated if FRC clusters are found at the vicinity of HEVs in the swelling LN as it
244 has been shown that *de novo* FRCs can derive from perivascular fibroblasts in the developing
245 spleen[42,43]. To this end, the CF was plotted as a function of the distance from HEVs. No
246 enrichment of clusters was found at these specific perivascular areas (Figure 6I).
247 To better understand the relationships between the measured parameters a correlation-
248 matrix was created (Figure 6J). As expected, the number of labeled FRCs correlated with the
249 number of observed clusters and the number of FRCs found in clusters, while the number of
250 clusters correlated well with the number of FRCs found in clusters. In the reactive LN *de novo*
251 MADM-events can occur, but our data indicate that these do not affect the CF as the CF is
252 independent of the number of labeled FRCs, and the relative numbers of FRC in clusters
253 remains unchanged in inflammation (Figure 6J, Figure S3H). LN volume was the best
254 determinant for the CF and also correlated well with the number of labeled FRCs, number of
255 clusters and FRCs in clusters (Figure 6J,K).

256 Together, these data show that FRCs expand in randomly distributed clusters and that FRC
257 growth correlates with LN volume (Figure 6K). This suggests that FRCs can expand in response
258 to local signals independent of their localization.
259
260 **Talin1 is required for FRC mechanosensing.**
261 Given our previous observations, mechanical forces appeared as an attractive feedback
262 parameter regulating FRC network growth. Mechano-coupling of fibroblasts to their
263 underlying matrix is mediated by integrins and their associated intracellular force-sensitive
264 adaptor molecule talin. FRCs express both Talin1 and Talin2 isoforms which play non-
265 redundant roles in integrin activation and force transduction[44]. We selectively deleted Talin1
266 in FRCs by generating Ccl19-*Cre; Talin1fl* ($FRC^{\Delta TLN1}$) mice.
267 Peripheral LNs of $FRC^{\Delta TLN1}$ mice were reduced in size and had lowered levels of the T-zone
268 chemokine CCL21 in the paracortex and the T cell zone was significantly reduced in size in
269 $FRC^{\Delta TLN1}$ LNs (FigureS4A-C). Within the T cell zone podoplanin (PDPN)+ $FRCs^{\Delta TLN1}$ still formed a
270 regularly interconnected network and expressed intercellular adhesion molecule 1 (ICAM-1)
271 and vascular cell adhesion molecule 1 (VCAM-1), arguing for regular differentiation (Figure
272 S4D). Within HEVs, CCL21 levels were unaffected (Figure S4B). Hence, despite the reduced
273 size, the basic organization and differentiation of the Talin1 deficient FRC network was
274 maintained. When $FRC^{\Delta TLN1}$ mice were immunized with KLH, LN swelling was substantial
275 (Figure7A) and during the initial four days after immunization, relative weight gain was
276 comparable to control mice. A mild reduction was only seen at D14. This demonstrates that
277 lymphocyte influx and proliferation were still occurring within the Talin deficient FRC
278 network, emphasizing the suitability of the genetic model to ask the principal question, if FRC
279 mechanosensing is required for network adaptation.
280 When we analyzed N:C YAP/TAZ ratio almost no $FRCs^{\Delta TLN1}$ showed a nuclear localization both
281 under homeostatic and reactive conditions (Figure 7B,C). This finding demonstrates that
282 Talin1 dependent mechanotransduction in FRCs is rate-limiting for YAP/TAZ nuclear
283 translocation and strongly indicate that $FRCs^{\Delta TLN1}$ lose their mechanosensitivity. To assess the
284 functional consequences for FRC network integrity we performed *in situ* network analysis. To
285 this end, 3D volumes of FRC networks were acquired from cleared thick vibratome slices and
286 network spacing was quantified using a 3D sphere-filling algorithm (Figure 7D,E). In
287 agreement with the previous 2D GAP analysis (Figure 2) the network of control mice widened

288 and remained intact at D4 of inflammation. The FRC$^{\Delta TLN1}$ network under homeostatic
289 conditions was widened compared to controls, but structurally intact. Upon immunization the
290 FRC$^{\Delta TLN1}$ network integrity became severely compromised, showing large FRC-free gaps
291 (Figure 7D,E & S4E). These defects were most apparent at D4 and partly recovered by D14 of
292 inflammation.
293 These data suggest that the FRC network in FRC$^{\Delta TLN1}$ mice failed to adapt to organ swelling
294 and partly disintegrated or ruptured. To investigate the fate of FRCs under these conditions
295 thick vibratome sections were stained for cleaved caspase 3 (cC3) and Ki67, to identify
296 apoptotic and proliferating FRCs, respectively (Figure 7F,G). These analyses showed little
297 apoptotic and proliferating FRCs in FRC$^{\Delta TLN1}$ and control mice under homeostatic conditions.
298 At D4 after immunization, the number of apoptotic FRCs per volume increased significantly
299 in FRC$^{\Delta TLN1}$ mice as compared to controls, while proliferation was similar in both control and
300 knockout. At D8, apoptotic FRCs per volume unit were still larger in FRC$^{\Delta TLN1}$ compared to
301 controls and proliferating FRCs were increased (Figure 7F,G).
302 These data indicate that compromised mechanosensing causes a severe dysregulation in
303 survival and proliferation of the FRC compartment, which leads to a loss of network integrity.
304 This finding is line with the idea that FRC remodeling is locally controlled by mechanical
305 feedback.
306
307 **Capsule fibrosis constrains lymph nodes at late time points**
308 Network analysis and tension measurements indicated that the FRC network reached a "new
309 equilibrium" two weeks after immunization, because it adopted its homeostatic
310 configuration. Nevertheless, effective resistance remained high at these late time points,
311 raising the question if another structure contributes to the force balance.
312 The LN capsule can be divided into two components: a floor that includes floor lymphatic
313 endothelial cells (fLECs) along with a basement membrane that connects to conduits, and a
314 roof that consists of ECM with embedded lymphoid fibroblasts to which ceiling lymphatic
315 endothelial cells (cLECs) adhere. We investigated the structural and mechanical properties of
316 the two capsule components in homeostatic and inflammatory conditions.
317 fLECs are sparsely labeled in FRC-mTmG mice, as is demonstrated by their double positivity
318 for mGFP and LYVE-1, and their location in the floor of the subcapsular sinus (SCS) (Figure
319 S5A). Since the SCS floor is densely populated by fLECs, we used this sparse labeling to our

320 advantage as it enabled the measurement of active tension on single fLECs *in vivo* using UV-
321 laser ablation (Figure 8A). We found that fLECs had high levels of basal tension that exceeded
322 those of FRCs (Figure 8B). Interestingly, after two days of inflammation fLECs showed reduced
323 tension that was reverted to homeostatic levels in the further swelling phase. Likewise, no
324 rise in active tension on the long time scale (D8-D14) was found on the capsule ECM following
325 UV laser ablation of explanted popliteal LNs (Figure S5B,C).
326 The absence of a continuous rise in active tension on the capsule floor and roof entails that
327 these components are being remodeled to keep up with the volumetric increase of the
328 swelling LN. The capsule was therefore assessed by histology in Prospero homeobox protein
329 1 (Prox1)- GFP mice in which the cytoplasm of all LECs is labeled with GFP. Additional 4',6-
330 diamidino-2-phenylindole (DAPI) and platelet-derived growth factor receptor- β (PDGFR-β)
331 staining allowed the measurement of capsule thickness and mesenchymal cell layers of the
332 capsule above the SCS in homeostasis and inflammation. We found that the capsule thickness
333 remained unchanged in the first four days of inflammation. Strikingly, the capsule thickness
334 increased ~14-fold from D8 to D14 of inflammation, forming a dense fibrotic layer between
335 the parenchyma and surrounding adipose and muscle tissue, while the SCS remained intact
336 (Figure 8C,D & Figure S5D).
337 We asked if such significant remodeling of the capsule resulted in changes in its mechanical
338 properties. To this end a micro-pipette with a small diameter was used to locally aspirate
339 ERTR7 labeled capsules of popliteal LN explants. Using Laplace's law, an effective Young's
340 modulus of the capsule was derived (Figure 8E). We found that the elastic modulus of the
341 capsule remained stable over the first eight days of inflammation but was doubled at D14
342 (Figure 8F). By multiplying the capsule thickness and Young's modulus of the capsule, we
343 derived the passive capsule tension; a measure of the amount of force necessary to enlarge
344 the whole thickness of the capsule by a certain length, i.e. the force needed to swell the LN.
345 The passive tension showed a substantive increase from D0 to D8 of inflammation and kept
346 rising to a massive 150-fold increase at D14 of inflammation (Figure 8G).
347 These data indicate that during a sustained immune response, tension dissipates from the
348 remodeling FRC network at the intermediary time scale (D4-D14), while the capsule remodels
349 and becomes thicker, stiffer and more resistant to swelling at the long time scale (D8-D14),
350 establishing a new force-equilibrium within the organ that resists further swelling (Figure 8H).
351

352 **Discussion**

353 Like glia cells of the nervous system, lymphatic stroma cells were long considered the passive
354 structural elements of the immune system. Only the last two decades revealed that the
355 stromal compartment decisively orchestrates immune cell encounters by providing trophic
356 and tactic cues and that in turn stromal cells dynamically respond to signals provided by the
357 immune cells[18,19]. Despite palpation of reactive LNs being part of every physical exam and LNs
358 being unmatched in their ability to change volume, the mechanical aspects of LN swelling
359 have never been directly addressed. By measuring organ mechanics across different time and
360 size scales we establish that reactive swelling of the LN is a multi-tier process controlled by
361 mechanical feedback. This allows the organ to expand in a step-wise controlled fashion,
362 without compromising its delicate architecture.

363 We demonstrate that upon inflammation, accumulating lymphocytes inflate the node and
364 initially stretch the FRC network. This is in line with previous findings that FRCs show an early
365 and transient increase in cell size[20]. Stretching puts tension on the ECM conduit as revealed
366 by a straightened configuration of its ECM fibrils. Although our ultrastructural analysis did not
367 show obvious ruptures of fibrillar collagen, Martinez et al.[45] detected gaps in the ECM (but
368 not the cellular) compartment of swelling LNs, raising the possibility that in some areas of the
369 LN, flexibility of the ECM cannot keep up with cellular deformation. Interestingly, both our
370 laser cutting experiments and the kinetics of nuclear shuttling of YAP/TAZ revealed that
371 compared to their ECM conduit, FRCs experience cytoskeletal tension only with a time delay
372 of two days. This is well in line with findings of the labs of Turley and Reis e Sousa, who showed
373 that early LN swelling is accompanied by a relaxation of the FRC system, allowing the network
374 to stretch[22,23]. Mechanistically, they demonstrated that CLEC-2 ligand expressed on activated
375 DCs binds podoplanin on FRCs and that this interaction relaxes actomyosin contractility within
376 the FRC myofibroblastic network. Such a transient FRC relaxation explains why tension-
377 increase of the ECM conduit precedes tension-increase of FRCs and implies that the FRC
378 cytoskeleton only experiences significant tension once the DC-mediated relaxation signals
379 fade after three to four days. Accordingly, FRCs show increased αSMA expression only after
380 the initial days of inflammation[20].

381 While the FRC network uses its intrinsic pliability to accommodate short-term volumetric
382 changes, sustained strain on the FRC cytoskeleton triggers the next stage of LN swelling, which
383 is characterized by actual growth and structural remodeling of the network. Our results on

384 genetic ablation of Talin1 in FRCs strongly support the idea that adhesion-dependent
385 mechanosensing is a critical feedback parameter that locally controls growth and survival of
386 the network, so that it reverts to its typical geometry, while being increased in size. In line
387 with these results, mice with a gain of function mutation in the mechanosensitive YAP/TAZ
388 pathway show fibrotic LNs with impaired FRC differentiation[46] and blockade of β1 integrin
389 triggered FRC apoptosis in swelling (but not in homeostatic) LNs[47]. A critical prerequisite of a
390 model where FRC mechanosensing locally controls network remodeling is that the FRC
391 responsiveness is not restricted to specific niches but rather distributed throughout the
392 organ. Our clonal analyses show that this is indeed the case and match results in follicular
393 dendritic cells and marginal reticular cells that were also shown to undergo clonal
394 expansion[48].
395 Beyond a week of structural adaptation the FRC network of the now massively enlarged LN
396 seemed to reach a new "mechanical equilibrium" as indicated by gap analysis, ECM
397 alignment, tension measurements and YAP/TAZ translocation. Nevertheless, bulk mechanical
398 properties of the LN did not return to homeostatic levels. They rather showed an elevated
399 effective resistance, indicating that another structure now countered the internal pressure
400 generated by the trapped lymphocytes. We thus turned to the capsule as the second major
401 stromal element and found that during these late stages, thickness and mechanical strength
402 of the capsule were massively increased, explaining resistance to further organ expansion.
403 Although capsule fibrosis is a characteristic histopathological descriptor of reactive LNs[49], its
404 mechanistic contributions are completely unexplored and future studies will hopefully show
405 how it contributes to sustained or chronic immune responses.
406 As the multi-tier model of LN swelling moves through a succession of check-points, it has the
407 advantage of being adaptable to very different types of swelling-scenarios. Transient swelling,
408 as it occurs e.g. during circadian fluctuations, might stretch the network, but is unlikely to
409 cause structural remodeling. In contrary, sustained immune responses with massive
410 lymphocyte trapping and germinal center reactions, might rely on a fibrotic strengthening of
411 the capsule in order to limit excessive expansion of the organ.
412

413 # Methods

414

415 **Animals**

416 All animal experiments are in accordance with the Austrian law for animal experiments.
417 Permission was granted by the Austrian Federal Ministry of Science, Research and Economy
418 (identification code: BMWFW 66.018/0010-WF/V/3b/2016). Mice were bred and maintained
419 at the local animal facility in accordance IST Austria Ethical Committee or purchased from
420 Charles River and maintained at the local animal facility in accordance with IST Austria Ethical
421 Committee. OT-II (Stock No: 004194) was bought from JAX. Ccl19-Cre mice have been
422 described previously[32]. MADM-7[39] and Talin1floxed[50] mice were provided by Simon
423 Hippenmeyer and David Critchley, respectively. All mice are on a C57BL/6J background, with
424 exception of MADM-7 which have a CD-1 background. Mice of both sexes between the age
425 of 6 to 20 weeks were used for experiments. For immunization, KLH protein was dissolved in
426 PBS to 5 mg/mL of and then mixed 1:1 with CFA (both Sigma-Aldrich) upon which 40 µL of the
427 immunization mixture was injected in footpads and flanks of draining popliteal and inguinal
428 LNS. LNs were harvested after various timepoint up to two weeks of induction of
429 immunization to be used for histology or explant experiments, or used for *in vivo* imaging
430 experiments. For LN cellularity manipulation experiments, mice were i.v. injected with 100 µg
431 α-CD62L (MEL14) (BioXCell), and control mice with PBS alone. For steady-state evaluation,
432 LNs were harvested 24h after injections were given, and for inflammation conditions
433 injections were given at onset of inflammation. Mice were anesthetized by isoflurane
434 inhalation (IsoFlo, Abbott) for all injection-based experiments, or anaesthetized with a
435 ketamine/xylazine/acepromazine mixture for *in vivo* imaging experiments.

436

437 **Histology and Imaging**

438 LNs were fixed in 4% paraformaldehyde (Electron Microscopy Sciences) in PB (0.1 M, pH 7.4)
439 at 4°C overnight. For cryosections, tissues were additionally embedded for 24h in a solution
440 of 30% glucose in PB (0.1 M, pH 7.4) before embedding and freezing in Tissue-Tek optimum
441 cutting temperature (OCT) compound (Sakura). Cryostat section (10-12 µm) were collected
442 on Superfrost/Plus glass slides (Thermo Fisher Scientific). Alternatively fixed tissues were

443 embedded in 4% low melting temperature agarose (Invitrogen) after fixation and 100-400 µm
444 sections were cut using a vibratome (VT1200S, Leica Microsystems).
445
446 Cryostat sections were air-dried for 2h at room temperature (RT) and washed in PBS. Sections
447 were blocked in SEABLOCK blocking buffer (Thermo Fisher Scientific) or in 5% bovine serum
448 albumin (BSA) (Thermo Fisher Scientific) in PBS for 1h, followed by incubation of primary
449 antibody solution diluted in 1% BSA/PBS for 1.5h at RT, 3 washing steps in PBS and subsequent
450 incubation of secondary antibody solution diluted in 1%BSA/PBS for 30 min at RT. Finally,
451 sections were washed three times in PBS, air-dried and mounted using Fluoromount-G with
452 DAPI (Thermo Fisher Scientific). Vibratome sections were blocked in 5% BSA/0.3%Triton-
453 x/PBS for 2h at RT under agitation followed by primary antibody incubation in 1%
454 BSA/0.3%Triton-x/PBS overnight at 4°C under agitation or for 2 days at RT in some cases. The
455 following day sections were washed three times in PBS. In case primary antibodies were not
456 conjugated with a fluorescent dye, samples were incubated with a secondary antibody in 1%
457 BSA/0.3%Triton-x/PBS for 4h at RT under mild agitation and subsequently washed three times
458 in PBS. All samples were then incubated in DAPI solution for 15 min and mounted on a glass
459 slide using Fluoromount-G (Thermo Fisher Scientific). The following primary antibodies were
460 used: α-CD3ε AF488 (17A2)(eBioscience), α-B220-Biotin (RA3-6B2) (eBioscience), α-Collagen
461 IV-Biotin (Abcam), α-CCL21-Biotin (R&D Systems), α-PDPN-Biotin (8.1.1) (eBioscience), α-
462 PDGFR-β (R&D Systems), α-YAP/TAZ (D24E4) (Cell Signal), α-cleaved Caspase 3-AF647
463 (Asp175) (Cell Signal), α-Ki67-APC (SolA15) (eBioscience), α-ICAM-1 (YN1/1.7.4) (BioXCell), α-
464 VCAM-1 (Phe25-Glu698) (R&D Systems), α-Fibroblast Marker-AF647 (ERTR7) (Santacruz
465 Biotech). α-PNAd (MECA-79) was derived from a concentrated hybridoma supernatant (kind
466 gift from Christine Moussion). The following secondary antibodies were used: Streptavidin-
467 Cy3 (Sigma-Aldrich), Streptavidin-AF647 (Jackson ImmunoResearch), chicken α-goat AF488
468 (Invitrogen), donkey α-rat AF647 (Jackson ImmunoResearch), donkey α-rabbit AF647 (Jackson
469 ImmunoResearch), goat α-mouse IgM AF647 (Invitrogen). Images were acquired on a Zeiss
470 LSM800 inverted confocal laser scanning microscope (CLSM) with the following objectives:
471 10x/NA0.45, 20x/NA0.8, 40x/NA1.2 Water and 63x/NA1.4 Oil Plan-APOCHROMAT.

472 Thick vibratome sections were in some cases cleared using the Ce3D protocol as described
473 previously[51]. Briefly, following antibody-staining samples were washed at RT on a shaker for

474 8h in washing buffer (PBS/0.3% Triton X-100, 0.5% 1-thioglycerol) which was refreshed after
475 4h. Next samples were cleared in freshly prepared Ce3D solution for 2x 1h, mounted in a µ-
476 dishes (Ibidi) and submerged in Ce3D solution. A cover-glass was placed on top to mount
477 cleared samples to the bottom of the well and the dish sealed with parafilm. Large 3D volumes
478 (xy:306x306 µm, z: 50-300 µm) were acquired from Ce3D cleared thick vibratome sections
479 using a spinning-disc microscope (Dragonfly, Andor) with a Apochromat LWD λS 40x/1.15
480 Water 0.60 mm WD objective.

481 **3D LSFM Sample Preparation and Imaging**

482 Terminally anesthetized Ccl19-cre hem; MADM-7$^{GT/TG}$ mice (mix C57BL/6J and CD1
483 background) were *in vivo* stained by retro-orbital injection of 40 µg/PBS mouse α-peripheral
484 node addressin (PNAd) concentrated hybridoma supernatant labeled with Atto-647N-NHS
485 (Atto-Tec). After 10 min, popliteal LNs were harvested and fixed in 4% paraformaldehyde
486 (Electron Microscopy Sciences) overnight at 4°C. Samples were washed in PBS, cleaned under
487 a stereomicroscope and cleared with the CUBIC protocol[52]. Briefly, samples were incubated
488 in CUBIC reagent 1 for 3 days at 37°C, which was replaced every 24h. Samples were then
489 washed with PBS, embedded in 2% low-meting temperature agarose (Sigma-Aldrich), and
490 sequentially dehydrated in 30% sucrose (Sigma-Aldrich) (1 day at 4°C) and 50% sucrose (2
491 days at 4°C). Finally, samples were incubated in CUBIC reagent 2 for 2 days at RT. Cleared
492 samples were imaged using a custom LSFM setup[53]. Acquired images were stitched using the
493 FIJI Grid/Collection-stitching plugin (Preibitsch Laboratory), despeckled and manually
494 registered using a custom-alignment-tool in Matlab (developed by Ekaterina Papusheva).
495

496 **FRC Cluster Analysis**

497 MADM-labeled cells were detected in 3D by employing a spot detection algorithm (Bitplane
498 Imaris) for each channel (tdTomato & GFP) separately. Chromatic aberrations and the
499 sequential nature of the image acquisition led to a channel misalignment which was corrected
500 for in the following way: the spot coordinates were exported from Imaris and treated as a
501 point cloud for each channel. These point clouds were then registered onto each other using
502 the Iterative closest point algorithm which corrected the shift and the rotation of the spectral
503 channels. Cells were then sorted into color classes (green (GFP), red (tdTomato) or yellow
504 (double positive) lineage). Red or green, if the spot existed solely in one of the point clouds,

505 or yellow if there were two corresponding spots in both channels that are closer than the
506 typical cell radius.
507
508 For the cluster analysis the LN outline and the HEVs were segmented in Imaris using the
509 surface detection feature. To correct errors in the cell detection, falsely detected spots from
510 autofluorescent structures outside of the LN volume were excluded from further analysis. In
511 order to avoid edge effects cells in a region 100 µm from the surface of the analyzed LNs were
512 excluded. FRC clusters were analyzed using a custom Matlab script utilizing a density-based
513 spatial clustering of applications with noise (DBSCAN) algorithm[40] in which FRCs were
514 represented as 3D spheres with a 12 µm diameter. An FRC cluster was defined as a minimum
515 of three FRCs of the same lineage (green or red) within a search-radius of 20 µm from each
516 FRC-sphere's surface.
517
518 To generate a random distribution (simulated FRCs), FRC-spheres were placed into the same
519 volume occupied by the real cells and excluded from HEV volumes. For each timepoint the
520 average of 10 distributions was used. The *cluster factor (CF)* was defined as *FRCs in*
521 *clusters/Total number of FRCs* divided by *Simulated FRCs in clusters/Total number of*
522 *simulated FRCs*.
523
524 **FRC Network GAP Analysis**
525 2D: A confocal laser scanning microscope with a 40x 1.2 water-objective (LSM800, Zeiss) was
526 used to acquire image stacks (range 10-30 µm and spaced at 1µm) with a field of view of
527 240x240 µm and a pixel size of 0.5 µm from T zones in which FRCs were labeled by mGFP
528 (Ccl19-Cre; mTmG mice). These were subsequently segmented using Ilastik software, the
529 result was then transformed into a binary image and noise was removed using a custom FIJI
530 script that utilized the particle detection algorithm. Binarized 3D image-stacks were then used
531 to measure the spacing (gaps) in the network by analyzing the pore-size distribution on
532 individual z-sections. The pore-size distribution was obtained analogously to the pore-size
533 analysis described in *Acton et al.*[22]. Starting with a circle size which corresponded to the
534 maximum gap of the network, circles were consecutively positioned into fitting corresponding
535 gaps of the network. The maximum circle size was determined from a distance transform of
536 the segmented network. Once no more circles of the maximum size could be placed into gaps

537 of the network, the disk size was reduced by one unit and the placement of the disks of
538 reduced sized commenced. This way, the gaps in the network were consecutively filled with
539 circles of decreasing size until the entirety of the gap area was filled. The results were then
540 averaged over the
541 3D: Large 3D volumes (xy:306x306 µm, z:50-500 µm) were acquired from Ce3D[51] cleared thick
542 vibratome sections using a Apochromat LWD λS 40x/1.15 Water 0.60 mm WD objective on a
543 spinning disc microscope (Dragonfly, Andor). Acquired 3D stacks were corrected for
544 fluorescent intensity in z-axis using 'bleach correction (histogram matching)' function in Fiji.
545 Imaris was then used to generate a 3D binary image of the FRC network by utilizing a surface
546 detection feature from the FRC-network fluorescent channel. A custom Matlab script was
547 subsequently used to fit 3D spheres in the 3D gaps of the network analog to the 2D approach.
548
549 **Parallel Plate Compression Experiments**
550 Explanted popliteal LNs were cleaned from adipose tissue under a stereomicroscope and
551 placed on a glass plate within the 37°C, RPMI 1640 (Invitrogen) filled incubation chamber of
552 a MicroSquisher device (CellScale). LNs were oriented to have their long axis along the field
553 of view of the camera. Compression was performed with a glass plate glued onto either a
554 0.304 or 0.408 mm diameter 40 GPa tungsten filament with a length of 60 mm. The glass slide
555 on the compression probe was coated with Poly-HEMA (Sigma-Aldrich) to reduce sticking of
556 the samples. LNs were then compressed by 25% of the initial height by lowering the upper
557 plate down in a timespan of 30 seconds. Lateral side-views of LNs were recorded up to 20-60
558 min after onset of the experiment, while resistant forces were measured on the upper plate.
559 Compression protocols, images and force acquisition were realized with the SquisherJoy
560 software (CellScale). Length, height, contact area and curvature of LNs were manually
561 measured before compression, and at the equilibrium timepoints using Fiji software. The
562 recorded compression force together with the measured geometrical parameters were used
563 to calculate volumes, Young's modulus, effective resistance and viscosity using a generalized
564 Kelvin model[27]. This was done as following:
565 The force required to maintain a constant strain of 25% on a LN was measured over time
566 (F(t)). The force initially peaks and then follows a relaxation curve which is fitted by a double
567 exponential decay curve. The simplest way to describe this bimodal dynamic is to incorporate
568 two dashpots with constants μ_1 and μ_2, and two springs with k1 and k2 constants. After 20-

569 60 min, the system reaches an equilibrium where the exerted force by the plate equals the
570 effective resistance of the LN (σ). Therefore, we have:

571 $$\sigma = \frac{F_{eq}/\pi {R_3}^2}{\left({}^{1}/_{R1} + {}^{1}/_{R2}\right)}$$

572 where F_{eq} is the equilibrium force at steady state and R1, R2 and R3 are derived from the
573 geometry of the LN.
574 To obtain the elastic modulus, the stress and strain need to be acquired:
575 Stress (s) is calculated from the force at equilibrium divided by plate contact area:

576 $$s = F_{eq}/\pi {R_3}^2$$

577 and the strain (ε) from:

578 $$\varepsilon = 1 - \frac{h_{eq}}{h_0}$$

579 where h_0 and h_{eq} correspond to the initial and equilibrium height of the compressed LN. From
580 here the elastic modulus (E) can be derived:

581 $$E = s/\varepsilon$$

582 Next, by fitting a double exponential decay to the force curve we obtain two time-scales, τ_1
583 and τ_2, where:

584 $$\tau_i = {}^{\mu_i}/_{k_i} \quad , i = 1, 2$$

585 Following up on the derivations of the equations as in *Forgacs et al.*[27], μ_1 and μ_2 can be
586 acquired readily, where μ_1 corresponds to the initial fast response in the order of seconds and
587 μ_2 to the slower response in the order of minutes, of which the latter one becomes relevant
588 for the rearrangements of the cells within LNs. Hence, we use μ_2 as our viscosity.
589 Measurements in which the LN was damaged during preparation (lymphocytes leaking out)
590 or moved/rolled during compression were excluded. In a few cases the viscosity could not be
591 determined (infinitely small) and were also excluded.
592 LN volumes were calculated from side-view images at *t=0* with the following formula:

593 $$V = \frac{4}{3}\,\pi\, R1\, \left(\frac{h_0}{2}\right)^2$$

594

595 **Micropipette Assay**

596 Popliteal LN explants were cleared from fat and incubated for 10 min in a 2 µg/mL ERTR7-
597 AF647 (Santa-Cruz) in RPMI 1640 (Invitrogen) to label the capsule. LNs were subsequently

598 placed on 3% methylcellulose coated glass bottom Petri dishes (MatTek) in RPMI and kept at
599 37°C, while imaged on an inverted Leica SP5 microscope using a 20x, 0.7NA objective (Leica
600 Microsystems). The local Young's Modulus of the capsule was measured with a glass
601 micropipette connected to a Microfluidic Flow Control System (Fluigent, Fluiwell), with
602 negative pressure ranging from 7-750 Pa, a pressure accuracy of 7 Pa and change rate of 200
603 $Pa*s^{-1}$. The micropipette equipment was mounted on a motorized micromanipulator
604 (Eppendorf, Transferman Nk2). Both systems were controlled by Dikeria software, Labview
605 (National Instruments). A fire polished micropipette with an inner diameter of 15 µm and flat
606 end (BioMedical instruments) was used for aspiration. The chosen diameter ensured that
607 mainly the capsule was probed and not the underlying parenchyma. While localizing the LN
608 capsule with the micropipette, the pressure inside the micropipette was kept at 0 Pa. For
609 measurements, a negative pressure of 750 Pa was applied, which resulted in the
610 instantaneous aspiration of the capsule. This pressure was chosen as lower pressure regimes
611 did not result in proper aspiration of the capsule. The tongue length of the capsule in the
612 micropipette upon aspiration was manually measured in Fiji from acquired movies. The
613 elasticity was subsequently calculated using the Laplace law:

614 $$E = \frac{\Delta P}{\left(\frac{h}{d}\right)^2}$$

615 With ΔP being the pressure difference between micropipette and atmosphere, h the height
616 of the measured tongue, and d the micropipette diameter.
617

618 **SEM Sample Preparation and Imaging**

619 Terminally ketamine/xylazine/acepromazine anesthetized mice were transcardially perfused
620 with PB (0.1 M, pH 7.4) and subsequently fixed with 2.5% glutaraldehyde and 2%
621 paraformaldehyde (Science Services) in PB (0.1 M, pH 7.4). LN samples were then dissected
622 and post-fixed in the same buffer for another hour at RT. They were dehydrated in a graded
623 ethanol series of 50%, 70%, 90%, 96%, 100% in H_2O for a minimum of 10 min per step and
624 subsequently kept overnight in fresh 100% ethanol at 4°C. Once in 100% ethanol, samples
625 were dried with a critical point dryer (EM-CPD300, Leica Microsystems), cut in half and coated
626 with a 4nm layer of platinum using a sputter coater (EM-ACE600, Leica Microsystems). The
627 samples were imaged with a field emission scanning electron microscope Merlin compact VP

628 (Carl Zeiss) at 3 kV. The signal was detected by an Everhart-Thornley type secondary electron
629 detector.
630
631 **STEM Tomography Sample Preparation**
632 Alkali maceration of LNs was performed as previously described[54,55]. Briefly, popliteal LNs
633 were isolated from 8–12 weeks old wt C57BL/6 mice and directly fixed in a 2.5%
634 glutaraldehyde and 2% paraformaldehyde in PB (0.1 M, pH 7.4) for a minimum of two weeks
635 at 4°C. Samples were then macerated in aqueous 2.5 M (10% w/v) NaOH solution for 5 days
636 at RT under mild agitation. Next sections were rinsed in H_2O under mild agitation for one to
637 two days until samples became pale. If results were not sufficient, the maceration step was
638 repeated.
639
640 Samples were then treated with 0.5% tannic acid (w/v) in PB (0.1 M, pH 7.4) two times 1h
641 each with freshly prepared solutions, washed in PB and treated with aqueous 1% osmium
642 tetroxide (w/v) for 30 min at 4°C. Samples were contrast enhanced with aqueous 1% uranyl
643 acetate (w/v) overnight at 4°C and Walton´s lead aspartate for 30 min at 60°C. Samples were
644 then dehydrated in graded ethanol, infiltrated with anhydrous propylene oxide and
645 embedded in hard-grade epoxy resin (Durcupan® ACM, Fluca). Samples were consecutively
646 infiltrated with a 3:1 mixture of anhydrous acetone and Durcupan® for 1h at 4°C, 1:1
647 aceton/Durcupan® for 1.5h at 4°C, 1:3 aceton/Durcupan® for 2h at 4°C and mere Durcupan®
648 overnight at RT. Samples were transferred to BEEM capsules (Electron Microscopy Sciences),
649 filled with freshly prepared Durcupan® and cured for 48h at 60°C.
650
651 **STEM Tomography Imaging**
652 Semi-thin sections were cut at 450 nm using an UC7 ultramicrotome (Leica Microsystems)
653 and collected onto formvar-coated 200-line bar grids + 1C/bar (Science Services, G200PB) and
654 coated with evaporated carbon to a thickness of 8nm. Grids were cut in half, mounted on a
655 Half-Mesh High Tilt holder (Jeol, EM-21010/Z09291THTR) and observed under a JEM 2800
656 scanning transmission electron microscope (Jeol) operated at 200 kV in STEM mode. To
657 compensate for focus, contrast and brightness, and stage shift during image tilt series
658 recording, an automated system was used comprising the STEM Recorder V3 Vers. 3.2.8.0
659 and the STEM Magica Controller Vers. 0.9.8.1 (both System In Frontier Inc.). Images were

collected at 2° intervals between +/-76° of single tilt axis. Magnification was x80k – x600k, image size 512x512 pixels giving a pixel sizes from 6.749463 nm/px to 0.899928 nm/px.

Conduit Stretching Quantification

STEM Tomography images were aligned by cross-correlation and 3D structure of area of interest computed by weighted back-projection using Composer software Vers. 3.0 (System In Frontier Inc.). A 3D Gaussian blur filter and background subtraction (rolling ball algorithm) pre-processing step were performed on the images using FIJI. The 3D image stacks were subsequently loaded into Imaris, and fibrils of conduits were manually traced using the Filament Tracer tool and exported to Matlab format using the Object Exporter (exported from Imaris as filaments). The overall orientation and curvature of the centerline of the entire conduit was approximated by fitting a cubic spline curve with four support points which minimized a hand-crafted cost function through all fibril track data. This cost function penalizes the distance of the desired centerline to the tracks, the total curvature of the centerline and the difference in length between it and the fibril bundles, and ensures that the support points are spaced evenly. In a few cases this spline curve was corrected by hand if it was found to not adequately represent the center line of the bundle. The alignment of the individual fibrils with respect to the centerline of the conduit was calculated as follows: The spline centerline was interpolated in a continuous fashion and the 3D orientation was calculated. Likewise, the tracks of individual fibrils were first smoothed to reduce tracing errors and the 3D orientation of each segment of the trace was calculated. The alignment angle A between the fibril is then given by the angle between the orientation of the segment and the orientation of the centerline at the point that is closest to the segment:

$$A = \mathrm{acos}\left(abs\left(\frac{\vec{v}_{fibril} \cdot \vec{v}_{Centerline}}{\left|\vec{v}_{fibril}\right| \times \left|\vec{v}_{Centerline}\right|} \right) \right)$$

UV-Laser Cutter Setup

The UV-laser cutter setup is based on a previously described layout[35,56]. In brief, a passively Q-switched solid-state 355 nm UV-A laser (Powerchip, Teem Photonics) with a repetition rate

689 of 1 kHz, pulse energy of 15 µJ, pulse-length of <350 ps and peak-power of 40 kW was used
690 in conjugation with a spinning disc microscope (Axio Observer Z1, Zeiss). The system is
691 controlled using custom-built software (LabView, National Instruments) enabling cutting in
692 3D. Typically 5% of the power is used to cut tissues.
693
694 **UV-Laser Ablation Experiments**
695 Tension on FRCs, fLECs and capsule ECM was measured by conducting laser ablations on an
696 inverted UV-laser ablation setup with a manufacturer 40x 1.2NA water immersion lens in
697 homeostatic and inflamed LNs. For all experiments 25 UV pulses at 1000 Hz to 40 equidistant
698 sites using 200 ms exposure time and frame rate were used to ablate and capture tissue recoil.
699 For FRC and LEC ablation, we established an intravital setup where Ccl19-Cre hem; mTmG
700 hom mice were anesthetized and intact inguinal LNs exposed using a skin flap surgery. The
701 paracortical site of the LN was mounted on a custom-made stage which allowed the LN
702 temperature to be regulated at 37°C. For capsule ECM ablation, popliteal LNs were harvested
703 and incubated in 100 µM TAMRA in RPMI 1640 solution (both Invitrogen) for 15 min at RT
704 and directly used for experiments. Explanted LNs were mounted at room temperature in a
705 glass bottom Petri dish (MatTek) in RPMI and prevented from floating using a 22x22 mm cover
706 glass topping.
707 Cuts were performed in either three z-planes spaced 1 µm apart along a length of either 10
708 µm for FRCs, or in one z-plane along 20 µm for fLECs and capsule ECM. FRC cuts were typically
709 performed at 10-20 µm depth underneath the capsule. Recoil of FRCs and LECs was quantified
710 from kymographs made in FIJI, while capsule ECM recoil was quantified using PIVlab in
711 Matlab. In the latter case, temporal recoil velocities were measured between bandpass
712 filtered pre- and consecutive post-cut frames by averaging the component of the calculated
713 velocity in the perpendicular direction to the cut, within an area of the surrounding cut site.
714
715 **YAP/TAZ Quantification**
716 The nuclear to cytoplasmic ration of stained YAP/TAZ in FRCs were measured from 3D sections
717 of peripheral LNs. In FIJI, FRCs were identified by the mGFP labeling and for each FRC the
718 average YAP/TAZ fluorescent intensity of the nucleus (identified by DAPI) was divided by the
719 average intensity of the adjacent cytoplasm of the cell body. In other cases, YAP/TAZ

720 localization was qualitatively assessed to contain to either contain a higher nuclear or
721 cytoplasmic YAP/TAZ intensity.
722
723 **CCL21 Quantification**
724 Cryosections containing both a control and $FRC^{\Delta TLN1}$ peripheral LN in a single section were
725 stained for CCL21 and pair-wise imaged using similar settings. The average fluorescent
726 intensities of CCL21 were then measured from paracortical areas and normalized to the
727 control.
728
729 **Proliferation and Apoptosis Measurements of FRCs**
730 Large 3D volumes (xy:306x306 µm, z: 50-150 µm) stained for either cleaved Caspase 3 or Ki67
731 were acquired from Ce3D cleared thick vibratome sections were corrected for fluorescent
732 intensity in z-axis using 'bleach correction (histogram matching)' function in Fiji. Imaris was
733 then used to generate a 3D isosurface of the FRC network by utilizing a surface detection
734 feature from the FRC-network fluorescent channel. The isosurface was then used to mask the
735 cleaved Caspase 3 and Ki67 channels so only the fluorescent signal within the FRC network
736 remained. Positive nuclei were then manually counted from 2D slice views and normalized
737 for per volume unit.
738
739 **Capsule Thickness Measurements**
740 The thickness of capsules was measured in vibratome sections of PROX1-GFP or wt mice,
741 stained for PDGFR-β and DAPI. The size of the capsule was then manually measured in FIJI
742 from the SCS to the surrounding adipose or muscular tissue from at least 3 locations and were
743 averaged per LN.
744
745 **Statistical Analysis**
746 All statistical analyses were performed in GraphPad Prism 8. P-values <0.05 were considered
747 significant.
748
749 **Software**

FIJI	Schindelin et al., 2012	https://fiji.sc/
Imaris	Bitplane	https://imaris.oxinst.com/packages
Excel	Microsoft	https://products.office.com/en-us/?rtc=1
Prism	GraphPad Software	https://www.graphpad.com/scientific-software/prism/
MATLAB	MATLAB Software	https://www.mathworks.com/products/matlab.html
Ilastik	Sommer et al., 2011	https://www.ilastik.org/
SquisherJoy	Cell Scale	https://www.cellscale.com/products/microtester/
Composer software	System In Frontier Inc.	https://temography.com/en/composer-en/
PIVlab	Thielicke and Stamhuis 2014	https://pivlab.blogspot.com/

Data availability

Data supporting the findings of this study are available from the corresponding authors upon.

Code availability

Code used for various analyses in this study are available from the corresponding authors upon request.

References

758

759 1. Lämmermann, T. & Sixt, M. The microanatomy of T-cell responses. *Immunol Rev* **221**, 26–
760 43 (2008).

761 2. Pham, T. H. M., Okada, T., Matloubian, M., Lo, C. G. & Cyster, J. G. S1P1 Receptor
762 Signaling Overrides Retention Mediated by Gαi-Coupled Receptors to Promote T Cell Egress.
763 *Immunity* **28**, 122–133 (2008).

764 3. Druzd, D. *et al.* Lymphocyte Circadian Clocks Control Lymph Node Trafficking and
765 Adaptive Immune Responses. *Immunity* **46**, 120–132 (2017).

766 4. Suzuki, K., Hayano, Y., Nakai, A., Furuta, F. & Noda, M. Adrenergic control of the adaptive
767 immune response by diurnal lymphocyte recirculation through lymph nodes. *J Exp Med* **213**,
768 2567–2574 (2016).

769 5. Luther, S. A., Tang, H. L., Hyman, P. L., Farr, A. G. & Cyster, J. G. Coexpression of the
770 chemokines ELC and SLC by T zone stromal cells and deletion of the ELC gene in the plt/plt
771 mouse. *Proc National Acad Sci* **97**, 12694–12699 (2000).

772 6. Matloubian, M. *et al.* Lymphocyte egress from thymus and peripheral lymphoid organs is
773 dependent on S1P receptor 1. *Nature* **427**, 355–360 (2004).

774 7. Mionnet, C. *et al.* High endothelial venules as traffic control points maintaining
775 lymphocyte population homeostasis in lymph nodes. *Blood* **118**, 6115–6122 (2011).

776 8. Andrian, U. H. von & Mempel, T. R. Homing and cellular traffic in lymph nodes. *Nat Rev*
777 *Immunol* **3**, 867–878 (2003).

778 9. Link, A. *et al.* Fibroblastic reticular cells in lymph nodes regulate the homeostasis of naive
779 T cells. *Nat Immunol* **8**, 1255–1265 (2007).

780 10. Knop, L. *et al.* IL-7 derived from lymph node fibroblastic reticular cells is dispensable for
781 naive T cell homeostasis but crucial for central memory T cell survival. *Eur J Immunol* **50**,
782 846–857 (2020).

783 11. Gorelik, L. *et al.* Normal B Cell Homeostasis Requires B Cell Activation Factor Production
784 by Radiation-resistant Cells. *J Exp Medicine* **198**, 937–945 (2003).

785 12. Cremasco, V. *et al.* B cell homeostasis and follicle confines are governed by fibroblastic
786 reticular cells. *Nat Immunol* **15**, 973–981 (2014).

787 13. Nakai, A., Hayano, Y., Furuta, F., Noda, M. & Suzuki, K. Control of lymphocyte egress
788 from lymph nodes through β2-adrenergic receptors. *J Exp Med* **211**, 2583–2598 (2014).

789 14. Devi, S. *et al.* Adrenergic regulation of the vasculature impairs leukocyte interstitial
790 migration and suppresses immune responses. *Immunity* **54**, 1219-1230.e7 (2021).

791 15. Kaldjian, E. P., Gretz, J. E., Anderson, A. O., Shi, Y. & Shaw, S. Spatial and molecular
792 organization of lymph node T cell cortex: a labyrinthine cavity bounded by an epithelium-
793 like monolayer of fibroblastic reticular cells anchored to basement membrane-like
794 extracellular matrix. *Int Immunol* **13**, 1243–1253 (2001).

795 16. Sixt, M. *et al.* The Conduit System Transports Soluble Antigens from the Afferent Lymph
796 to Resident Dendritic Cells in the T Cell Area of the Lymph Node. *Immunity* **22**, 19–29 (2005).

797 17. Bajénoff, M. *et al.* Stromal Cell Networks Regulate Lymphocyte Entry, Migration, and
798 Territoriality in Lymph Nodes. *Immunity* **25**, 989–1001 (2006).

799 18. Perez-Shibayama, C., Gil-Cruz, C. & Ludewig, B. Fibroblastic reticular cells at the nexus of
800 innate and adaptive immune responses. *Immunol Rev* **289**, 31–41 (2019).

801 19. Krishnamurty, A. T. & Turley, S. J. Lymph node stromal cells: cartographers of the
802 immune system. *Nat Immunol* **21**, 369–380 (2020).

803 20. Yang, C.-Y. *et al.* Trapping of naive lymphocytes triggers rapid growth and remodeling of
804 the fibroblast network in reactive murine lymph nodes. *Proc National Acad Sci* **111**, E109–
805 E118 (2014).

806 21. McConnell, I. & Hopkins, J. Lymphocyte traffic through antigen-stimulated lymph nodes.
807 I. Complement activation within lymph nodes initiates cell shutdown. *Immunology* **42**, 217–
808 23 (1981).

809 22. Acton, S. E. *et al.* Dendritic cells control fibroblastic reticular network tension and lymph
810 node expansion. *Nature* **514**, 498–502 (2014).

811 23. Astarita, J. L. *et al.* The CLEC-2–podoplanin axis controls the contractility of fibroblastic
812 reticular cells and lymph node microarchitecture. *Nat Immunol* **16**, 75–84 (2015).

813 24. Chyou, S. *et al.* Coordinated Regulation of Lymph Node Vascular–Stromal Growth First
814 by CD11c+ Cells and Then by T and B Cells. *J Immunol* **187**, 5558–5567 (2011).

815 25. Gregory, J. L. *et al.* Infection Programs Sustained Lymphoid Stromal Cell Responses and
816 Shapes Lymph Node Remodeling upon Secondary Challenge. *Cell Reports* **18**, 406–418
817 (2017).

818 26. Majumder, S. *et al.* IL-17 metabolically reprograms activated fibroblastic reticular cells
819 for proliferation and survival. *Nat Immunol* **20**, 534–545 (2019).

820 27. Forgacs, G., Foty, R. A., Shafrir, Y. & Steinberg, M. S. Viscoelastic Properties of Living
821 Embryonic Tissues: a Quantitative Study. *Biophys J* **74**, 2227–2234 (1998).

822 28. Delarue, M. *et al.* Self-driven jamming in growing microbial populations. *Nat Phys* **12**,
823 762–766 (2016).

824 29. Jain, R. K., Martin, J. D. & Stylianopoulos, T. The Role of Mechanical Forces in Tumor
825 Growth and Therapy. *Annu Rev Biomed Eng* **16**, 321–346 (2014).

826 30. Mao, Y. *et al.* Differential proliferation rates generate patterns of mechanical tension
827 that orient tissue growth. *Embo J* **32**, 2790–2803 (2013).

828 31. Gallatin, W. M., Weissman, I. L. & Butcher, E. C. A cell-surface molecule involved in
829 organ-specific homing of lymphocytes. *Nature* **304**, 30–34 (1983).

830 32. Chai, Q. *et al.* Maturation of Lymph Node Fibroblastic Reticular Cells from
831 Myofibroblastic Precursors Is Critical for Antiviral Immunity. *Immunity* **38**, 1013–1024
832 (2013).

833 33. Madisen, L. *et al.* A robust and high-throughput Cre reporting and characterization
834 system for the whole mouse brain. *Nat Neurosci* **13**, 133–140 (2010).

835 34. Smutny, M., Behrndt, M., Campinho, P., Ruprecht, V. & Heisenberg, C.-P. Tissue
836 Morphogenesis, Methods and Protocols. *Methods Mol Biology* **1189**, 219–235 (2014).

837 35. Colombelli, J., Grill, S. W. & Stelzer, E. H. K. Ultraviolet diffraction limited nanosurgery of
838 live biological tissues. *Rev Sci Instrum* **75**, 472–478 (2004).

839 36. Panciera, T., Azzolin, L., Cordenonsi, M. & Piccolo, S. Mechanobiology of YAP and TAZ in
840 physiology and disease. *Nat Rev Mol Cell Bio* **18**, 758–770 (2017).

841 37. Zong, H., Espinosa, J. S., Su, H. H., Muzumdar, M. D. & Luo, L. Mosaic Analysis with
842 Double Markers in Mice. *Cell* **121**, 479–492 (2005).

843 38. Contreras, X. *et al.* A genome-wide library of MADM mice for single-cell genetic mosaic
844 analysis. *Cell Reports* **35**, 109274 (2021).

845 39. Hippenmeyer, S., Johnson, R. L. & Luo, L. Mosaic Analysis with Double Markers Reveals
846 Cell-Type-Specific Paternal Growth Dominance. *Cell Reports* **3**, 960–967 (2013).

847 40. Ester, M., Kriegel, H.-P., Sander, J. & Xu, X. A density-based algorithm for discovering
848 clusters in large spatial databases with noise. in *Proceedings of the Second International*
849 *Conference on Knowledge Discovery and Data Mining* (eds. Simoudis, E., Han, J. & Fayyad,
850 U.) 226–231 (AAAI Press, 1996).

851 41. Bailey, N. T. J. *The Elements of Stochastic Processes with Applications to the Natural*
852 *Sciences*. (Wiley-Interscience, 1990).

853 42. Schaeuble, K. *et al.* Perivascular Fibroblasts of the Developing Spleen Act as LTα1β2-
854 Dependent Precursors of Both T and B Zone Organizer Cells. *Cell Reports* **21**, 2500–2514
855 (2017).

856 43. Cheng, H.-W. *et al.* Origin and differentiation trajectories of fibroblastic reticular cells in
857 the splenic white pulp. *Nat Commun* **10**, 1739 (2019).

858 44. Austen, K. *et al.* Extracellular rigidity sensing by talin isoform-specific mechanical
859 linkages. *Nat Cell Biol* **17**, 1597–1606 (2015).

860 45. Martinez, V. G. *et al.* Fibroblastic Reticular Cells Control Conduit Matrix Deposition
861 during Lymph Node Expansion. *Cell Reports* **29**, 2810-2822.e5 (2019).

862 46. Choi, S. Y. *et al.* YAP/TAZ direct commitment and maturation of lymph node fibroblastic
863 reticular cells. *Nat Commun* **11**, 519 (2020).

864 47. Kumar, V. *et al.* A Dendritic-Cell-Stromal Axis Maintains Immune Responses in Lymph
865 Nodes. *Immunity* **42**, 719–730 (2015).

866 48. Jarjour, M. *et al.* Fate mapping reveals origin and dynamics of lymph node follicular
867 dendritic cells. *J Exp Med* **211**, 1109–1122 (2014).

868 49. Mills, S. *Histology for Pathologists*. (LWW, 2019).

869 50. Nieswandt, B. *et al.* Loss of talin1 in platelets abrogates integrin activation, platelet
870 aggregation, and thrombus formation in vitro and in vivo. *J Exp Medicine* **204**, 3113–3118
871 (2007).

872 51. Li, W., Germain, R. N. & Gerner, M. Y. High-dimensional cell-level analysis of tissues with
873 Ce3D multiplex volume imaging. *Nat Protoc* **14**, 1708–1733 (2019).

874 52. Susaki, E. A. *et al.* Whole-Brain Imaging with Single-Cell Resolution Using Chemical
875 Cocktails and Computational Analysis. *Cell* **157**, 726–739 (2014).

876 53. Abe, J. *et al.* Light sheet fluorescence microscopy for in situ cell interaction analysis in
877 mouse lymph nodes. *J Immunol Methods* **431**, 1–10 (2016).

878 54. OHTANI, O. Three-dimensional Organization of the Connective Tissue Fibers of the
879 Human Pancreas: A Scanning Electron Microscopic Study of NaOH Treated-Tissues. *Arch*
880 *Histol Japon* **50**, 557–566 (1987).

881 55. Ushiki, T., Ohtani, O. & Abe, K. Scanning electron microscopic studies of reticular
882 framework in the rat mesenteric lymph node. *Anatomical Rec* **241**, 113–122 (1995).

883 56. Behrndt, M. *et al.* Forces Driving Epithelial Spreading in Zebrafish Gastrulation. *Science*
884 **338**, 257–260 (2012).

885

Acknowledgements

This research was supported by the Scientific Service Units of IST Austria through resources provided by the Bio Imaging, Electron Microscopy, Preclinical and Life Science Facilities. We thank Christine Moussion for providing anti-PNAd antibody, Simon Hippenmeyer and David Critchley for respectively donating transgenic MADM-7 and Talin1floxed mice, and Ekaterina Papusheva for providing a custom 3D channel alignment script. This work was supported by European Research Council grant ERC-CoG-72437.

Contributions

F.P.A. designed experiments, and performed all *in vivo* and *ex vivo* experiments with assistance of M.H., M.B., S.S and G.K.; J.A. cleared samples and did light-sheet imaging, F.P.A. did all other fluorescent imaging. W.A.K. processed samples for electron tomography, and W.A.K., T.C. and F.P.A. acquired tomograms. F.P.A. did all data processing and analysis with help of R.H., S.S. and G.K; R.H. wrote all custom analysis scripts. S.H. and E.H. aided in the interpretation of MADM and mechanical data, respectively. S.L discussed data. M.S. directed the study, F.P.A. and M.S. wrote the manuscript, and all authors critically reviewed the manuscript.

Ethics declarations

The authors declare no competing interests.

902 **Figure Legends**

903

904 **Figure 1.** The reactive lymph node resists swelling. (**a**) Side-view focus-stack of popliteal LNs
905 in homeostasis (D0) and inflammation (D14). Scale bar = 500 µm. (**b**) Volumes of swelling LNs
906 calculated from 2D-side views over the course of two-week following onset of immunization.
907 Means±SEM are connected (blue line) and a linear regression line (dashed) has been fitted to
908 the data. (**c-d**) Overview of the stress-relaxation experiment on explanted popliteal LNs (D2
909 of inflammation depicted). (**c**) Measured geometrical parameters are annotated on 2D-side
910 images acquired during a measurement. Scale bar = 300 µm. (**d**) The stress relaxation curve
911 is given by the measured force over time from which the equilibrium force (long timescale)
912 parameter), viscosity (medium timescale) and Young's Modulus (short timescale) relaxation
913 parameters are derived. (**e-g**) Quantification of tissue properties in homeostasis (D0) and
914 inflammation (D2, D4, D8, D14) derived from the stress relaxation curve and geometrical
915 properties. Each datapoint represents a single measured LN. Measurements are pooled from
916 LNs harvested from at least 5 mice and multiple experiments. Mean±SEM. (**e**) Quantification
917 of the effective resistance. (**f**) Quantification of the viscosity. (**g**) Quantification of the Young's
918 Modulus. For statistical analysis see Supplementary Information, table 1. *P<0.05, **P<0.01,
919 ****P<0.0001.

920

921 **Figure 2**. Lymphocyte numbers generate pressure and drive lymph node swelling. (**a-j**)
922 Analysis of stress-relaxation experiments on explanted LNs. Each datapoint represents a
923 single measured LN. Measurements are pooled from LNs harvested from at least 5 mice and
924 multiple experiments. Mean±SEM are given. (**a**) Side-view of explanted homeostatic LNs from
925 mice treated with anti-CD62L or PBS. Scale bars = 300 µm. Dashed lines depict the outline of
926 LNs. (**b**) Quantification of LN volume. (**c**) Quantification of the effective resistance. (**d**)
927 Quantification of the viscosity. (**e**) Quantification of the Young's Modulus. (**f**) Side-view of
928 explanted D4 inflamed LNs from wt and OTII mice treated with anti-CD62L or PBS. Scale bars
929 = 400 µm. Dashed lines depict the outline of LNs. (**g**) Quantification of LN volumes. (**h**)
930 Quantification of the effective resistance. (**i**) Quantification of the tissue viscosity. (**j**)
931 Quantification of the Young's Modulus. For statistical analysis see Supplementary

932 Information, table 1. ns, not significant. ns, not significant. *P<0.05, **P<0.01, ***P<0.001,
933 ****P<0.0001.
934
935 **Figure 3.** The FRC network stretches upon lymph node swelling. (**a**) Overview of the FRC
936 network gap analysis. Left: mGFP labeled FRCs (green), middle: segmented FRC network
937 (white), right: gaps (randomly colored circles) in the FRC network. Scale bar = 20 µm. (**b**)
938 Representative images of FRC networks gaps in homeostasis (D0) and inflammation (D2, D4,
939 D8 and D14). (**c**) Averaged and smoothed distribution of FRC network fitted circle distribution
940 plotted as the Weighted Area Fraction as a function of the fitted circle diameter. (**d**)
941 Quantification of the mean fitted-circle diameter. Each datapoint represents the average
942 value of 10-30 analyzed consecutive sections of an acquired 3D volume. Means for each
943 timepoint are depicted as a black line. Data are for each timepoint pooled from 5 popliteal or
944 inguinal LNs from at least 3 mice and 2 separate experiments. For statistical analysis see
945 Supplementary Information, table 1. ***P<0.001, ****P<0.0001.
946
947 **Figure 4.** Conduits are stretched in the swelling lymph node. (**a**) Overview of STEM
948 tomography acquisition of macerated LN samples. Images show the fibrillar collagen of T zone
949 conduits at a single tilt angle, and a maximum intensity projection crop of a 3D conduit
950 reconstructed from multiple tilting angles. (**b**) Representative 3D reconstructions of fibrillar
951 collagen (blue) from macerated conduits at homeostasis (day 0) and inflammation (D2, D4
952 and D14) in which the conduit center line (yellow) and tracked fibril segments (grey) are
953 annotated. (**c**) Visual representation of the conduit fibril alignment analysis of an imaged 3D
954 conduit volume. Angles of individual fibril segments (thick colored lines) with the center line
955 of the conduit (dashed black line) are measured at multiple points along the fibril segment
956 (thin colored lines) and averaged per fibril segment. (**d**) Quantification of conduit fibril
957 alignment with center line. Each datapoint represents an individual fibril segment. Means are
958 depicted as black lines. For statistical analysis see Supplementary Information, table 1. ns, not
959 significant. ***P<0.001, ****P<0.0001.
960
961 **Figure 5.** FRC network tension increases upon lymph node swelling. (**a**) Overview of *in vivo*
962 UV-laser cut experiment of the FRC network. Inguinal LNs from FRC-mGFP mice are surgically
963 exposed and kept hydrated at 37°C. A high UV-laser cuts the FRC network along 10 µm at 3

964 different planes after which the local recoil of the FRC network is imaged. Scissor and line
965 indicate cutting location and arrows the recoiling FRC network. Scale bars = 20 µm. (**b**)
966 Representative example of FRC network recoil. Images depict stills from before (t=-1s),
967 directly after (t=0s) and late after (t=6.2s) cutting (scale bars = 5 µm), with corresponding
968 kymograph along the recoil axis (scale bar x-axis = 1s, y-axis = 2 µm). Scissor and line indicate
969 cutting location and arrows the recoiling FRC network. Dashed lines in kymograph indicate
970 slopes used to calculate the recoil velocity, and vertical white line the cut. (**c**) Quantification
971 of recoil velocity from kymographs. Each datapoint represents a single FRC network cut. Data
972 is pooled from 3-4 animals and at least 2 experiments per analyzed timepoint. Means±SEM
973 are depicted and connected with a line. (**d**) 3D view of the FRC network and stained for
974 YAP/TAZ. Stack size 20 µm. Scale bar = 20 µm. (**e**) Representative examples of YAP/TAZ
975 nuclear and cytoplasmic localization. N:C = nuclear to cytoplasmic fluorescent intensity ratio.
976 (**f**) Quantification of YAP/TAZ N:C ratio. Dashed line indicates an equal ratio. Each datapoint
977 corresponds to a single measured FRC. Measurements are taken from a total of 3 LNs per
978 analyzed timepoint from at least two separate experiments. Means±SEM are depicted and
979 connected with a line. For statistical analysis see Supplementary Information, table 1. ns, not
980 significant. *P<0.05, **P<0.001, ****P<0.0001.
981
982 **Figure 6**. FRCs in the swelling lymph node undergo distributed clonal expansion. (**a**) Schematic
983 overview of the sparse mosaic analysis with double markers (MADM) labeling approach for
984 FRC cluster imaging. (**b-k**) Quantification of light sheet images from cleared LNs in
985 homeostasis (D0) and inflammation (D4 and D8). All graphs depict the mean±SD. Each
986 datapoint represents a single popliteal LN. LNs are retrieved from at least 3 mice and 2
987 separate experiments for each condition. (**b**) LN volumes. (**c**) Numbers of MADM labeled FRCs.
988 (**d**) Numbers of FRCs found in clusters. (**e**) Number of clusters. (**f**) 3D view of HEVs (grey) and
989 smoothed convex-hull of cluster volumes (randomly colored) in a homeostatic (D0) and
990 inflamed (D4) LN, scale bar = 200 µm (**g**) Frequency distribution of FRC cluster sizes found in
991 observed and simulated data in homeostasis (D0) and inflammation (D4 and D8). (**h**)
992 Quantification of the cluster factor (CF) between homeostatic (D0) and inflamed LNs (D4 and
993 D8). (**i**) Number of FRC clusters in homeostatic (D0) and inflamed LNs (D4 and D8) plotted as
994 a function of the distance from the nearest HEV. (**j**) Correlation-matrix of paired variables
995 assessed in the cluster analysis. Spearman correlation: *p*-values are given and the correlation-

996 coefficients are color-coded. (**k**) CF plotted as a function of the LN volume. A spline-fit is
997 plotted through the data-points. For statistical analysis see Supplementary Information, table
998 1. ns, not significant. **P<0.01, ***P<0.001, ****P<0.0001.
999
1000
1001 **Figure 7.** Talin1 is required for FRC mechanosensing. (**a**) Quantification of LN weights in
1002 homeostasis and following inflammation (D4 and D14) in control and FRC$^{\Delta Talin1}$ mice. Each
1003 datapoint represents a single LN. Data is pooled from at least 5 mice from multiple
1004 experiments per condition. Insert depicts the grow curves of the plotted data fitted with a
1005 non-linear regression function. Mean±SEM. (**b**) T zone FRC network of FRC-mGFP (control)
1006 and FRC$^{\Delta Talin1}$-GFP mice stained for YAP/TAZ. Enlargements depict representative examples of
1007 the N:C of YAP/TAZ. Scale bars = 10 µm. (**c**) Quantification of YAP/TAZ localization in FRCs of
1008 control and FRC$^{\Delta Talin1}$ mice in homeostasis (D0) and at inflammation (D4). Mean±SEM. (**d**)
1009 Representative 3D images of 3D network analysis of control and FRC$^{\Delta Talin1}$ mice in homeostasis
1010 (D0) and following inflammation (D4 and D14). Imaged stack size: 100-300 µm. Scale bars =
1011 50 µm. (**e**) Quantification of FRC network analysis as shown in **d**. Left: average weighted
1012 volume fraction plotted as function of the sphere diameter. Right: average sphere diameter
1013 for all conditions. Each datapoint represents an individual LN from at least 3 mice and 2
1014 experiments per condition. Means are depicted by black lines. (**f**) Quantification of cleaved
1015 Caspase3+ FRCs from FRC-mGFP (control) and FRC$^{\Delta Talin1}$-GFP mice in homeostasis (D0) and
1016 inflammation (D4 and D8). Each datapoint represents a single LN. Data pooled from 3 mice
1017 per timepoint. Images depict the identification of an apoptotic FRC. Scale bar = 3 µm. (**g**)
1018 Quantification of Ki67+ FRCs from FRC-mGFP (control) and FRC$^{\Delta Talin1}$-GFP mice in homeostasis
1019 (D0) and inflammation (D4 and D8). Each datapoint represents a single LN. Images depict the
1020 identification of a proliferating FRC. Scale bar = 3 µm. Data pooled from 3 mice per timepoint.
1021 Mean±SD. For statistical analysis see Supplementary Information, table 1. ns, not significant.
1022 *P<0.05, **P<0.01, ***P<0.001, ****P<0.0001.
1023
1024 **Figure 8.** Capsule fibrosis constrains lymph nodes at late timepoints. (**a**) Overview of intravital
1025 UV-laser cut experiments of the SCS fLECs. Inguinal LNs from FRC-mGFP mice, in which SCS
1026 fLECs are sparsely labeled with a mGFP are surgically exposed. A high UV-laser cuts the cell
1027 along 20 µm in one plane after which the local recoil is imaged. Images depict stills from

before (t=-1s), directly after (t=0s) and late after (t=10.2s) cutting (scale bars = 5 µm), with corresponding kymograph along the recoil axis (scale bar x-axis = 1s, y-axis = 2 µm). Scissor and line indicate location of cut and arrows the recoiling cell. Dashed lines in kymograph indicate slopes used to calculate the recoil velocity, and vertical white line the cut. (**b**) Quantification of experiments as described in **a** for homeostatic (D0) and inflamed (D2, D4, D8, D14) LNs. Each datapoint represents a recoil-measurement of a single fLEC. Data pooled from 3 mice and at least two experiments. Mean±SEM are depicted and connected with a line. (**c**) Representative confocal images of LN capsules from PROX1-GFP mice in homeostasis (D0) and inflammation (D4, D8 and D14), in which LECs are labeled by a cytoplasmic GFP. Mesenchymal cells are stained for PDGFR-β, and nuclei are counterstained with DAPI. Scale bars = 20 µm. (**d**) Quantification of the capsule thickness measured from the SCS as depicted in **c.** Each datapoint represents the average of 3 measurements per LN. Mean±SEM are connected with a line. Data pooled from 5 LNs derived from 3 mice per timepoint. (**e**) Overview of micro-pipette assay for capsule stiffness measurements. Capsules of explanted popliteal LNs are labeled by brief incubation with Alexa Fluor 647-conjugated anti-ERTR7 antibody, upon which a small diameter glass pipette is placed on the capsule and a defined negative pressure applied. The ECM 'tongue' entering the pipette is subsequently measured. The local effective Young's Modulus of the capsule is derived using Laplace's law. Scale bar = 50 µm. (**f**) Quantification of measurements as described in **e** for homeostatic (D0) and inflamed (D2, D4, D8 and D14) LNs. Each datapoint represents the average of 3 measurements per LN. Mean±SEM are connected with a line. Data pooled from 5 LNs derived from 3 mice per timepoint. (**g**) Quantification of the Capsule swelling resistance as measured by the Passive Tension, given by multiplying the capsule thickness and Young's modulus from **d** and **f**, respectively. Each datapoint represents a single LN. Mean±SEM are connected with a line. (**h**) Schematic of the mechanical dynamics of the swelling LN. For statistical analysis see Supplementary Information, table 1. ns, not significant. **P<0.01, ***P<0.001.

1055 ## Supplementary Figure Legends

1056 **Supplementary Figure 1.** (**a**) Quantification of popliteal LN volumes calculated from 2D side
1057 views in homeostasis (D0) and inflammation (D2, D4, D8, D14) acquired from parallel plate
1058 compression experiments. Mean±SEM. (**b**) Relation between calculated volumes and
1059 measured weights of popliteal LNs in homeostasis and inflammation. A regression line is
1060 fitted. (**c**) Example of a double-exponential force fit (red line) on a stress-relaxation
1061 measurement. Arrow indicates the force at equilibrium (F_{eq}). (**d**) Average of stress-relaxation
1062 curves for all measured conditions. Mean±SEM. (**e**) Schematic representation of the
1063 generalized Kelvin model and formulas used to calculate tissue properties from parallel plate
1064 stress-relaxation experiments. Adapted from *Forgacs et al.*. (**f**) SEM image of packed
1065 lymphocytes in the LN paracortex. Scale bar = 2 µm. For statistical analysis see Supplementary
1066 Information, table 1. **P<0.01, ****P<0.0001.

1067 **Supplementary Figure 2.** (**a**) Schematic of LN processing for STEM tomography of T zone
1068 conduits. (**b**) Example of a macerated conduit imaged by STEM in which the characteristic D-
1069 period of collagen fibrils can be observed. Scale bar = 500 µm. (**c**) Examples of a T zone conduit
1070 at different tilting angles acquired by STEM tomography. (**d**) Schematic of a computed weight
1071 back projection to reconstruct a 3D volume of a conduit from differential tilting angles.

1072 **Supplementary Figure 3.** (**a**) Schematic of the MADM labeling principle. Rare
1073 interchromosomal recombination in the G2 cell cycle phase following x-segregation of
1074 chromosomes labels FRCs with either a cytoplasmic tdTomato or GFP. (**b**) Sparse labeling of
1075 FRCs. Scale bar = 200 µm. (**c**) 3D fluorescent intensity images of GFP labeled FRCs and *in situ*
1076 labeled HEVs by anti-PNAd-ATTO647n antibody. (**d**) Quantification of the MADM labeling
1077 distribution in homeostasis (D0) and inflammation (D4 and D8). Each datapoint represents a
1078 single LN. Mean±SD. (**e**) Overview of the labeling of HEVs and mapping of labeled FRCs (only
1079 tdTomato+FRCs are shown) at D4 of inflammation. The enlarged image depicts the mapping
1080 of individual FRCs by a grey sphere at the center of each cell. Scale bars = 200 µm. (**f**) Formula
1081 for the calculation of the cluster factor (CF) per LN. (**g**) Quantification of the average distance
1082 to the nearest neighbor (NN) of both mapped FRCs and randomly localized FRCs from
1083 simulations in homeostasis (D0) and inflammation (D4 and D8). Means are depicted by black
1084 lines. (**h**) Quantification of relative numbers of MADM-labeled FRCs found in clusters in both

1085 homeostasis (D0) and inflammation (D4 and D8). Mean±SD. For statistical analysis see
1086 Supplementary Information, table 1. ns, not significant. **P<0.01, ***P<0.001.

1087 **Supplementary Figure 4.** (**a**) Quantification of steady-state popliteal and inguinal LN weights
1088 from control and FRC$^{\Delta Talin1}$ mice. Each datapoint represents a measured LN. Images show a
1089 representative inguinal LN for each condition. Scale bars = 1 mm. (**b**) Quantification of steady-
1090 state T zone CCL21 protein as measured *in situ* by fluorescent intensity following staining for
1091 CCL21. Measurements are taken from histological sections from 5 LNs of 3 mice for each
1092 condition. Mean±SEM. Scale bars = 20 µm. (**c**) T zone and B-cell follicles in steady-state
1093 popliteal LNs from control and FRC$^{\Delta Talin1}$ mice stained for CD3 (T cells) and B220 (B cells). Scale
1094 bars = 200 µm. (**d**) ICAM-1, PDPN, VCAM and merged staining from steady-state popliteal LN
1095 T zones from control and FRC$^{\Delta Talin1}$ mice. Scale bars = 20 µm. (**e**) Overview of the T zone FRC
1096 network in homeostasis (D0) and inflammation (D4 and D14) between FRC-mGFP (control)
1097 and FRC$^{\Delta Talin1}$-mGFP mice stained for collagen IV. Scale bar = 50 µm. For statistical analysis see
1098 Supplementary Information, table 1. *P<0.05, ****P<0.0001.

1099 **Supplementary Figure 5.** (**a**) Ccl19-Cre; mTmG mice sparsely label fLECs of the SCS. Zoomed
1100 window depict the SCS with LECs brightly labeled with tdTomato (mTdT) and the sparsely
1101 labeled fLEC (mGFP), given by the double positive labeling with the fLEC-marker LYVE-1 (gray).
1102 (**b**) Overview of the UV-laser cut experiment on TAMRA labeled capsule ECM of explanted LNs
1103 in homeostasis (D0) and inflammation (D2, D4, D8, D14), which faithfully represents capsule
1104 ECM as observed in alkali macerated LNs imaged by STEM and SEM. Particle imaging
1105 velocimetry (PIV) was used to measure displacement of structures above and below the cut
1106 site from band-pass filtered images. Recoil displacement is depicted by orange vectors. Scale
1107 bar STEM image = 5 µm, SEM image = 1 µm, fluorescent TAMRA-labeled image = 20 µm. (**c**)
1108 Quantification of recoil velocities of capsule cuts from experiments on homeostatic (D0) and
1109 inflamed (D2, D4, D8, D14) LNs as described in **b**. Each datapoint represents a single cut.
1110 Between 14 and 24 cuts were taken per measured timepoint from at least 5 LNs from two
1111 animals and at least two separate experiments. Mean+SEM connected by a line. (**d**)
1112 Representative histological examples of LN capsules from PROX1-GFP mice in homeostasis
1113 and D14 of inflammation, stained for PDGFR-β and counterstained with DAPI. Scale bars =
1114 200 µm. For statistical analysis see Supplementary Information, table 1. *P<0.05, **P<0.01.

1115 ## Supplementary Movie

1116 **Supplementary Movie 1.** Example of low (homeostasis; D0) and high tension (Inflammation;
1117 D4) of the FRC network as given by the recoil speed following *in vivo* UV-laser cutting in
1118 surgically exposed inguinal LNs of FRC-mGFP mice.

Figure 1

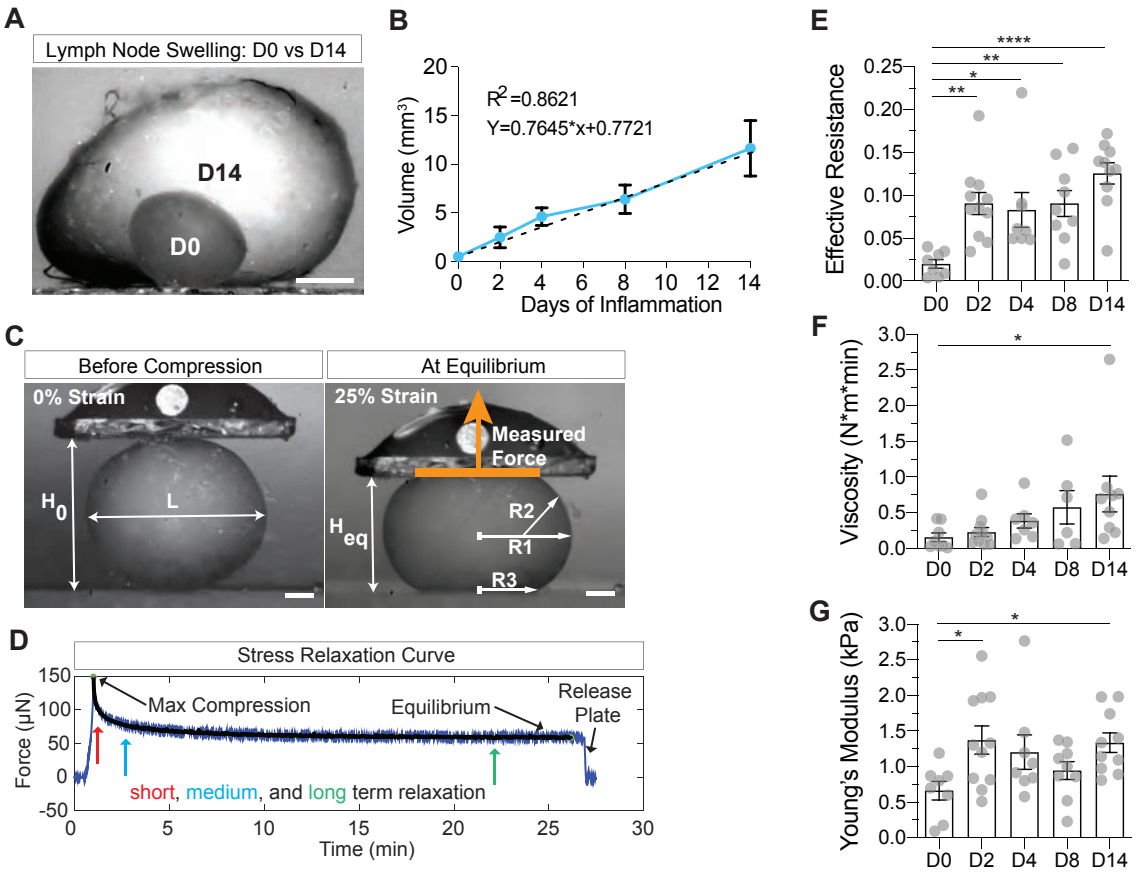
A
Lymph Node Swelling: D0 vs D14
D14
D0
B
R2=0.8621
Y=0.7645*x+0.7721
Volume (mm3)
Days of Inflammation
C
Before Compression
At Equilibrium
0% Strain
25% Strain
Measured Force
H0
L
Heq
R2
R1
R3
D
Stress Relaxation Curve
Force (µN)
Max Compression
Equilibrium
Release Plate
short, medium, and long term relaxation
Time (min)
E
Effective Resistance
D0 D2 D4 D8 D14
F
Viscosity (N*m*min)
G
Young's Modulus (kPa)

Figure 2

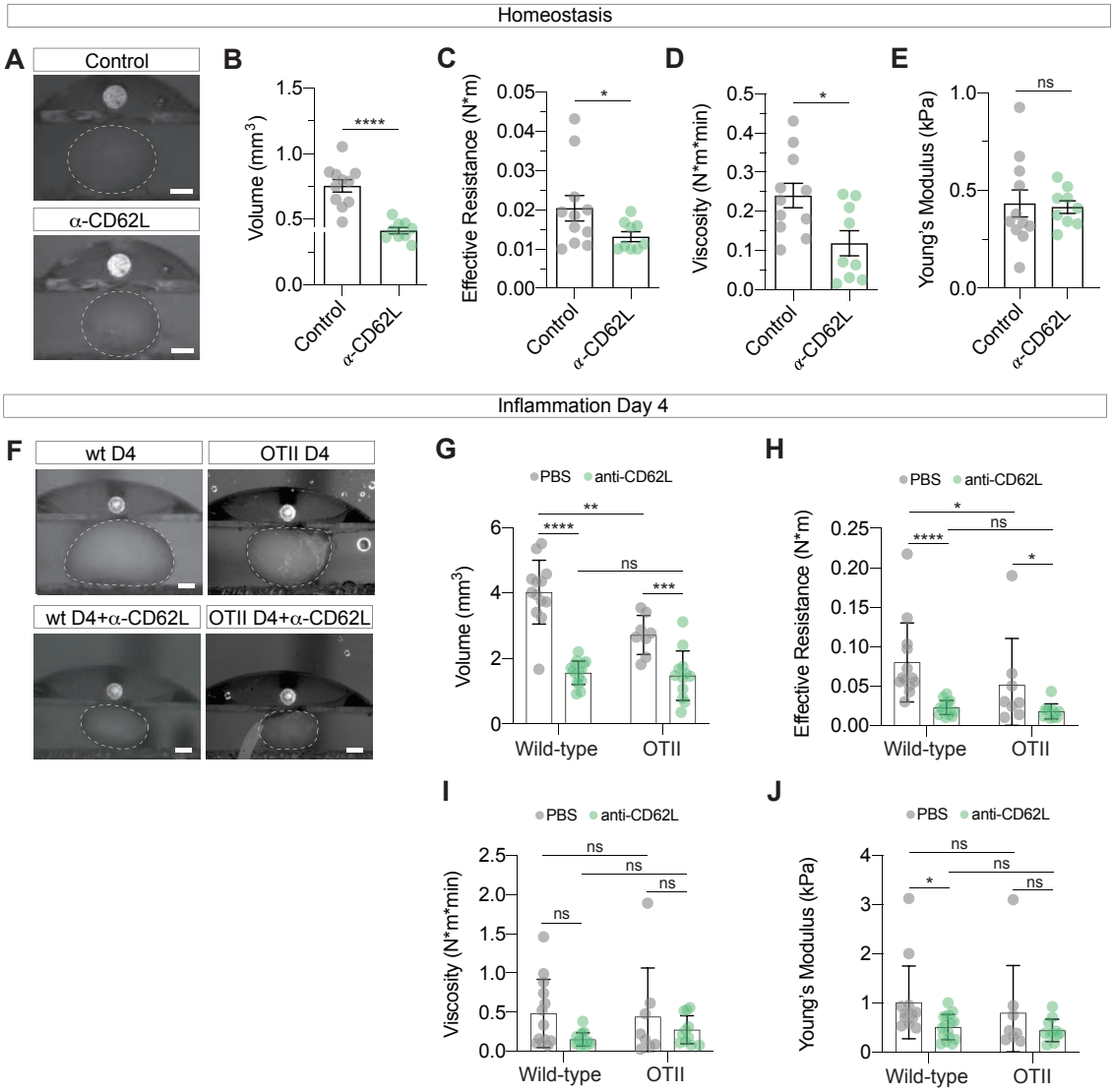
Homeostasis
A
Control
α-CD62L
B
Volume (mm3)
****
Control
α-CD62L
C
Effective Resistance (N*m)
*
D
Viscosity (N*m*min)
*
E
Young's Modulus (kPa)
ns
Inflammation Day 4
F
wt D4
OTII D4
wt D4+α-CD62L
OTII D4+α-CD62L
G
PBS
anti-CD62L
Volume (mm3)
Wild-type
OTII
H
Effective Resistance (N*m)
I
Viscosity (N*m*min)
J
Young's Modulus (kPa)

Figure 3

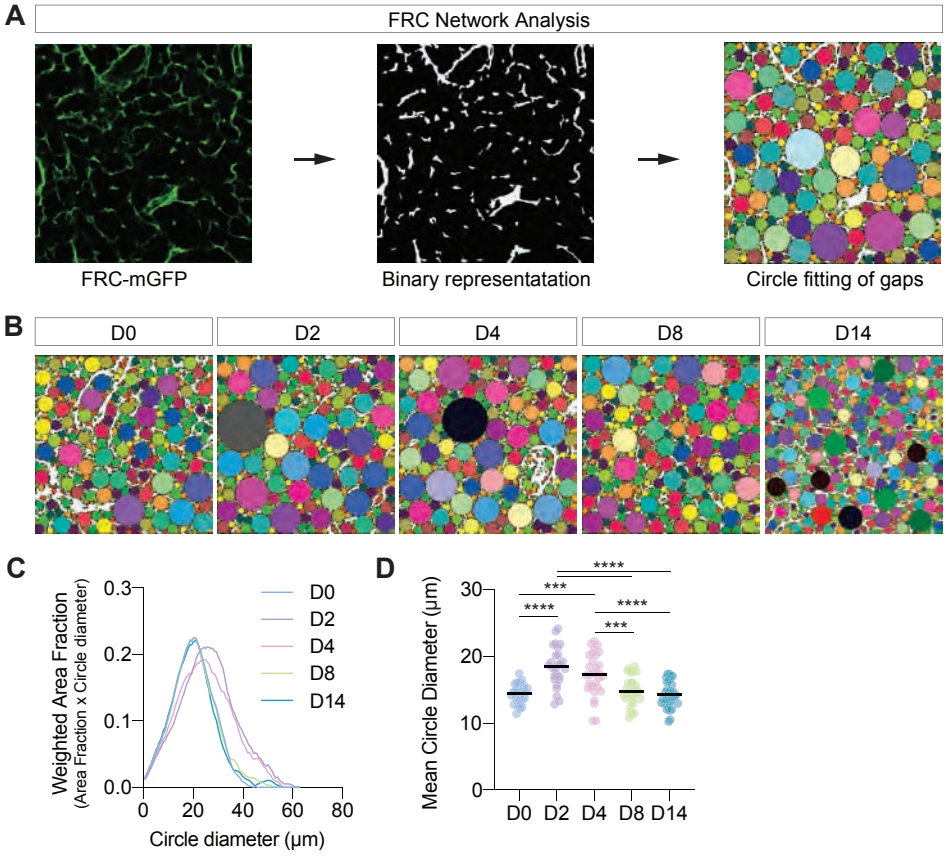
A
FRC Network Analysis
FRC-mGFP
Binary representatation
Circle fitting of gaps
B
D0
D2
D4
D8
D14
C
Weighted Area Fraction
(Area Fraction x Circle diameter)
0.3
0.2
0.1
0.0
0
20
40
60
80
Circle diameter (µm)
D0
D2
D4
D8
D14
D
Mean Circle Diameter (µm)
30
20
10
0
****
***
****
****
***
D0
D2
D4
D8
D14

Figure 4

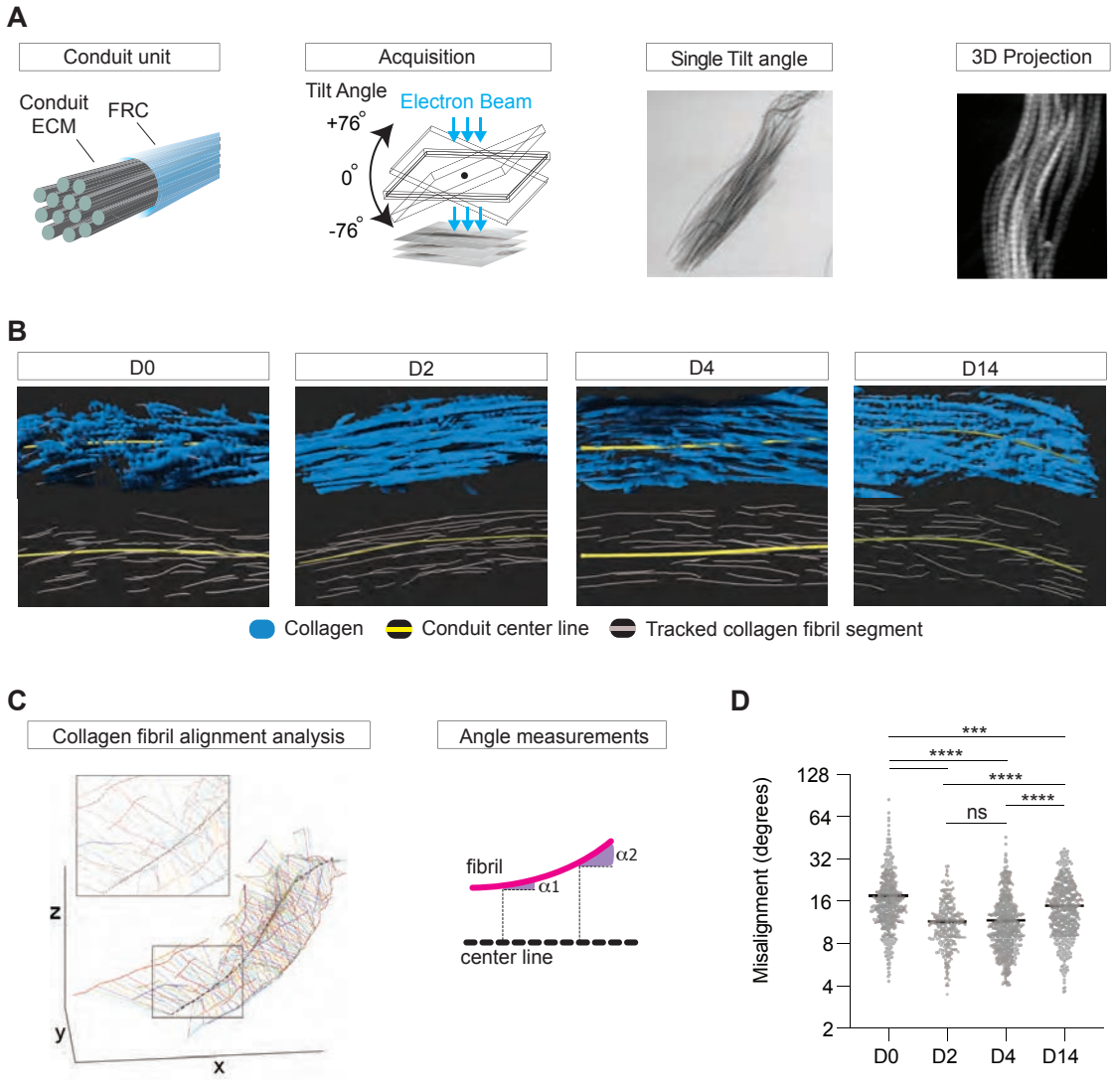
A
Conduit unit
Conduit ECM
FRC
Acquisition
Tilt Angle
Electron Beam
+76°
0°
-76°
Single Tilt angle
3D Projection
B
D0
D2
D4
D14
Collagen
Conduit center line
Tracked collagen fibril segment
C
Collagen fibril alignment analysis
Angle measurements
fibril
α1
α2
center line
z
y
x
D
Misalignment (degrees)
128
64
32
16
8
4
2
D0
D2
D4
D14
***
****
****
ns
****

Figure 5

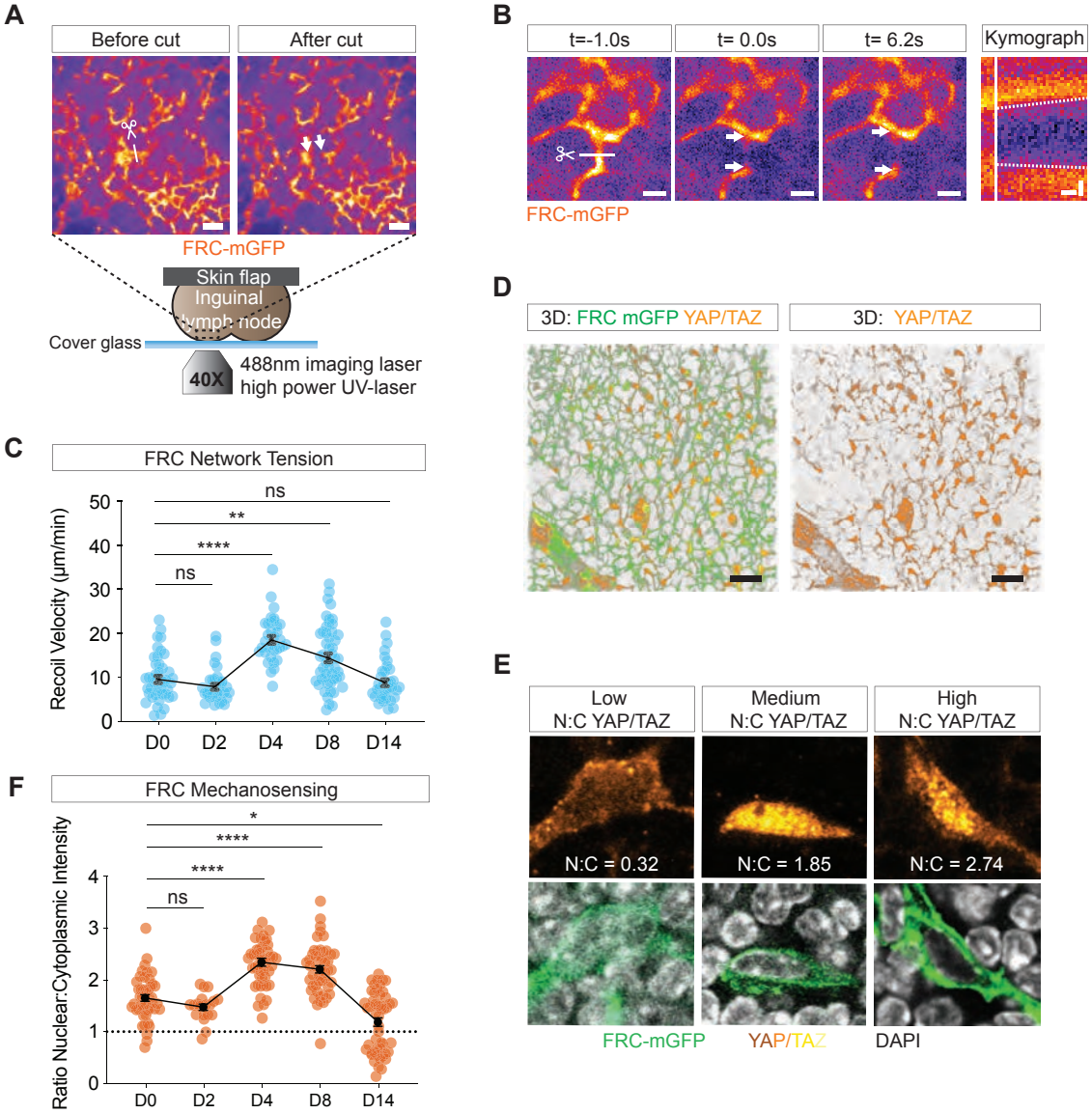
A
Before cut
After cut
FRC-mGFP
Skin flap
Inguinal
lymph node
Cover glass
40X
488nm imaging laser
high power UV-laser
B
t=-1.0s
t= 0.0s
t= 6.2s
Kymograph
FRC-mGFP
C
FRC Network Tension
Recoil Velocity (µm/min)
ns
**
****
ns
D0
D2
D4
D8
D14
D
3D: FRC mGFP YAP/TAZ
3D: YAP/TAZ
E
Low
N:C YAP/TAZ
Medium
N:C YAP/TAZ
High
N:C YAP/TAZ
N:C = 0.32
N:C = 1.85
N:C = 2.74
FRC-mGFP
YAP/TAZ
DAPI
F
FRC Mechanosensing
Ratio Nuclear:Cytoplasmic Intensity
*
****
****
ns
D0
D2
D4
D8
D14

Figure 6

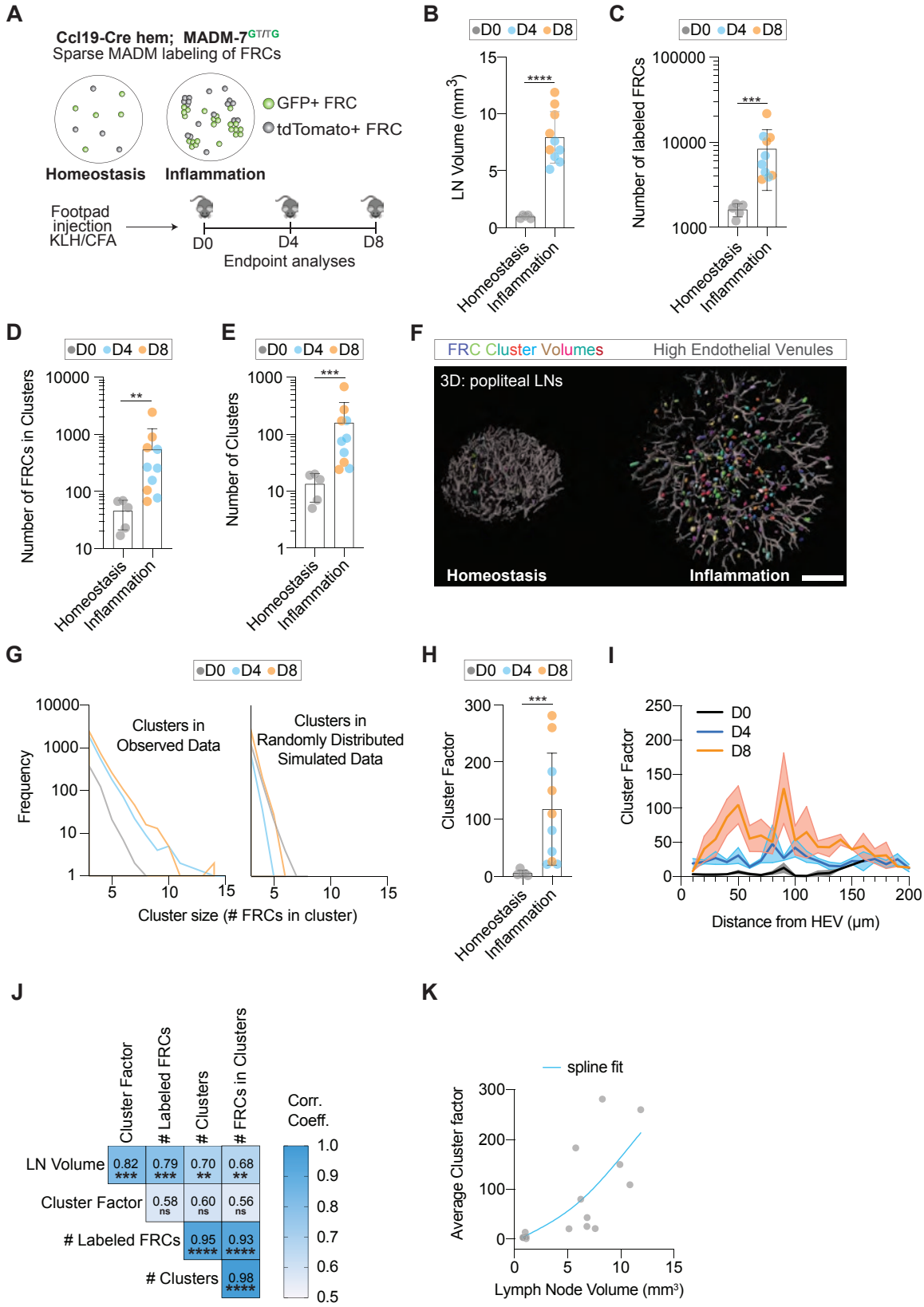
A
Ccl19-Cre hem; MADM-7GT/TG
Sparse MADM labeling of FRCs
GFP+ FRC
tdTomato+ FRC
Homeostasis
Inflammation
Footpad injection KLH/CFA
D0
D4
D8
Endpoint analyses
B
D0 D4 D8
LN Volume (mm3)
Homeostasis
Inflammation
C
Number of labeled FRCs
D
Number of FRCs in Clusters
E
Number of Clusters
F
FRC Cluster Volumes
High Endothelial Venules
3D: popliteal LNs
Homeostasis
Inflammation
G
Frequency
Clusters in Observed Data
Clusters in Randomly Distributed Simulated Data
Cluster size (# FRCs in cluster)
H
Cluster Factor
I
Distance from HEV (µm)
J
Cluster Factor
Labeled FRCs
Clusters
FRCs in Clusters
Corr. Coeff.
LN Volume
Cluster Factor
Labeled FRCs
Clusters
K
spline fit
Average Cluster factor
Lymph Node Volume (mm3)

Figure 7

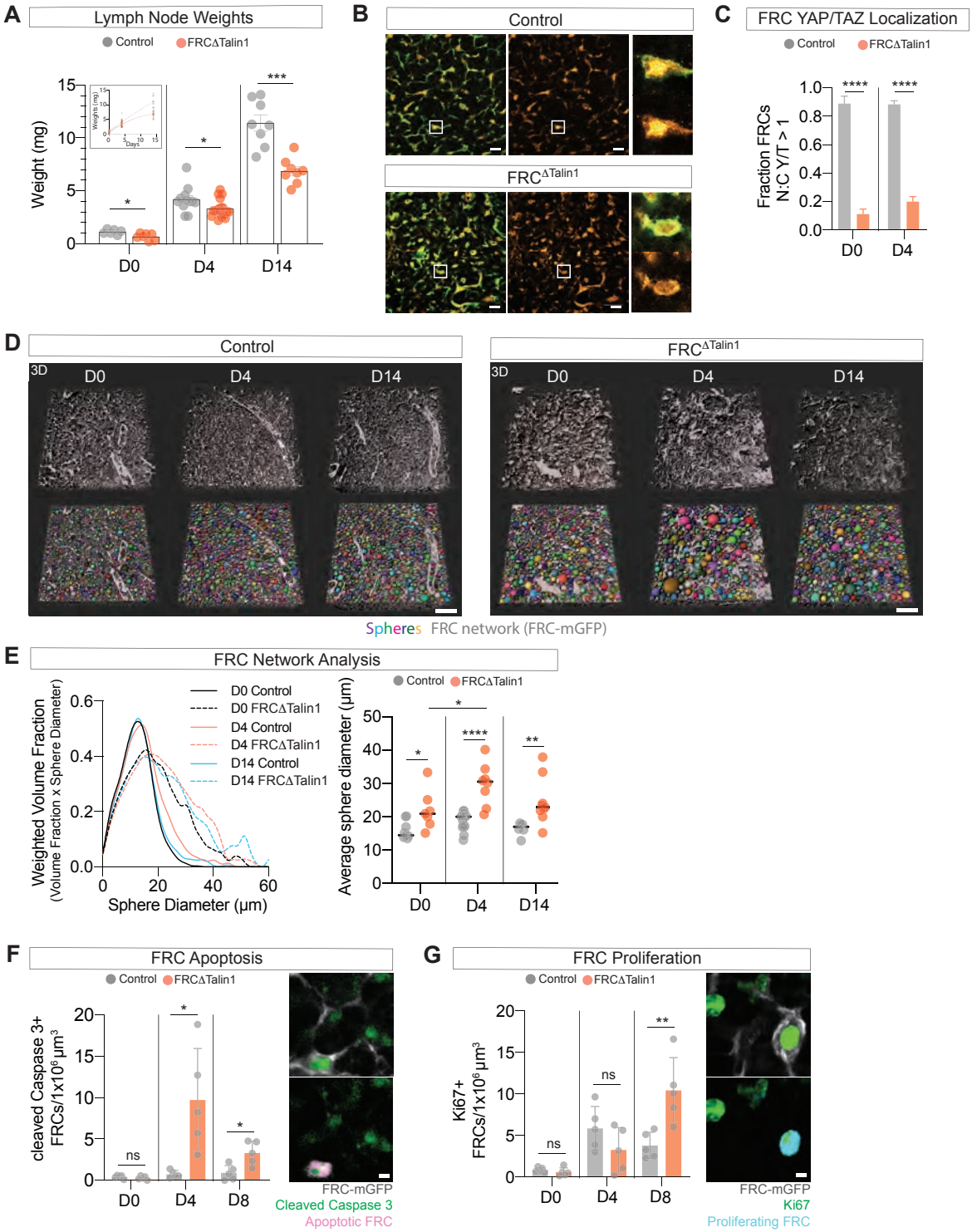
A
Lymph Node Weights
Control
FRCΔTalin1
Weight (mg)
D0
D4
D14
B
Control
FRCΔTalin1
C
FRC YAP/TAZ Localization
Control
FRCΔTalin1
Fraction FRCs N:C Y/T > 1
D0
D4
D
Control
FRCΔTalin1
3D
D0
D4
D14
Spheres
FRC network (FRC-mGFP)
E
FRC Network Analysis
D0 Control
D0 FRCΔTalin1
D4 Control
D4 FRCΔTalin1
D14 Control
D14 FRCΔTalin1
Weighted Volume Fraction (Volume Fraction x Sphere Diameter)
Sphere Diameter (µm)
Control
FRCΔTalin1
Average sphere diameter (µm)
D0
D4
D14
F
FRC Apoptosis
Control
FRCΔTalin1
cleaved Caspase 3+ FRCs/1x10^6 µm^3
ns
D0
D4
D8
FRC-mGFP
Cleaved Caspase 3
Apoptotic FRC
G
FRC Proliferation
Control
FRCΔTalin1
Ki67+ FRCs/1x10^6 µm^3
ns
D0
D4
D8
FRC-mGFP
Ki67
Proliferating FRC

Figure 8

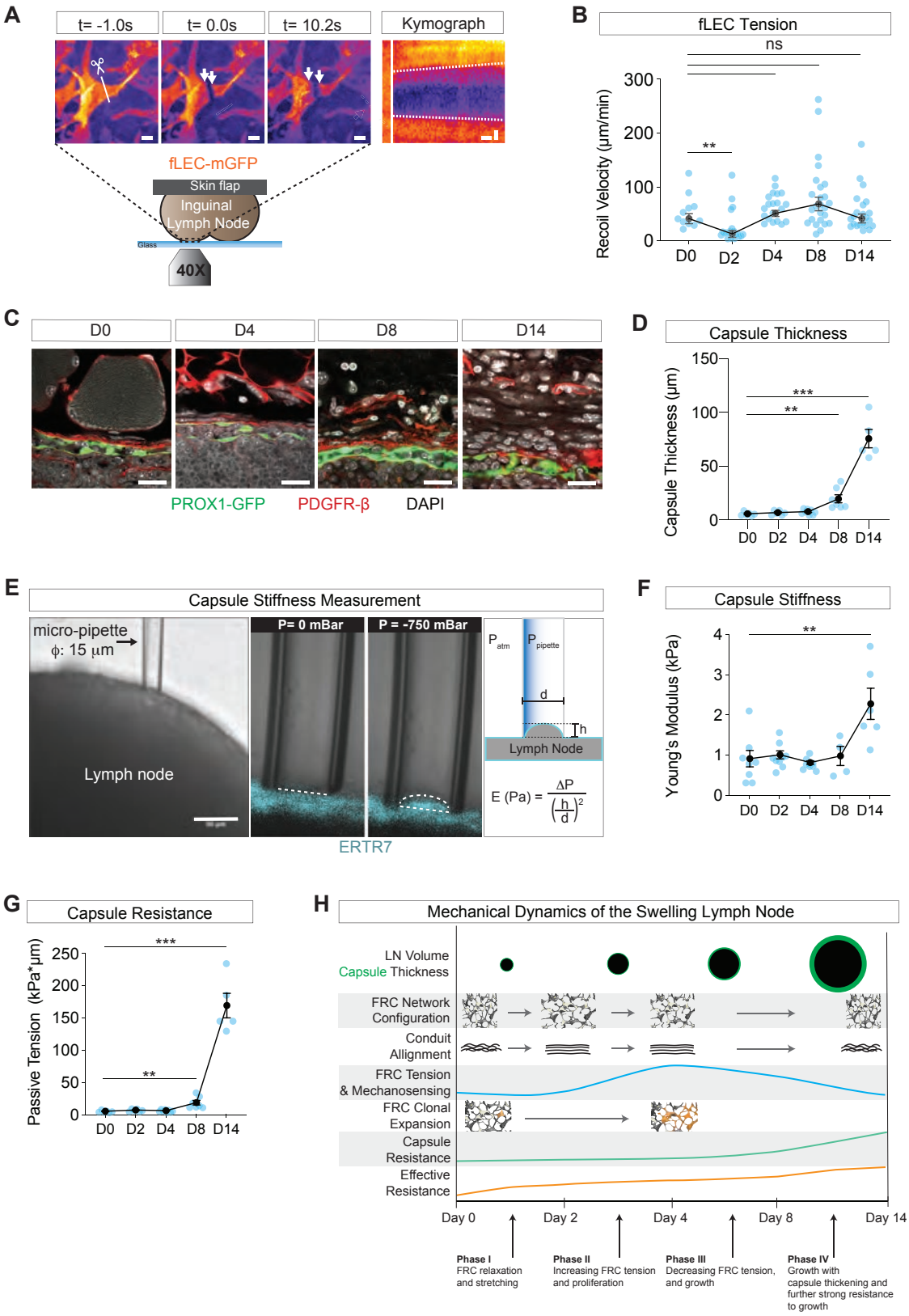
A
t= -1.0s
t= 0.0s
t= 10.2s
Kymograph
fLEC-mGFP
Skin flap
Inguinal Lymph Node
Glass
40X
B
fLEC Tension
ns
**
Recoil Velocity (µm/min)
300
200
100
0
D0
D2
D4
D8
D14
C
D0
D4
D8
D14
PROX1-GFP
PDGFR-β
DAPI
D
Capsule Thickness
Capsule Thickness (µm)
150
100
50
0
***
**
D0
D2
D4
D8
D14
E
Capsule Stiffness Measurement
micro-pipette
ϕ: 15 µm
Lymph node
P= 0 mBar
P = -750 mBar
P atm
P pipette
d
h
Lymph Node
E (Pa) = ΔP / (h/d)²
ERTR7
F
Capsule Stiffness
Young's Modulus (kPa)
4
3
2
1
0
**
D0
D2
D4
D8
D14
G
Capsule Resistance
Passive Tension (kPa*µm)
250
200
150
100
50
0
***
**
D0
D2
D4
D8
D14
H
Mechanical Dynamics of the Swelling Lymph Node
LN Volume
Capsule Thickness
FRC Network Configuration
Conduit Allignment
FRC Tension & Mechanosensing
FRC Clonal Expansion
Capsule Resistance
Effective Resistance
Day 0
Day 2
Day 4
Day 8
Day 14
Phase I
FRC relaxation and stretching
Phase II
Increasing FRC tension and proliferation
Phase III
Decreasing FRC tension, and growth
Phase IV
Growth with capsule thickening and further strong resistance to growth

Supplementary Figure 1

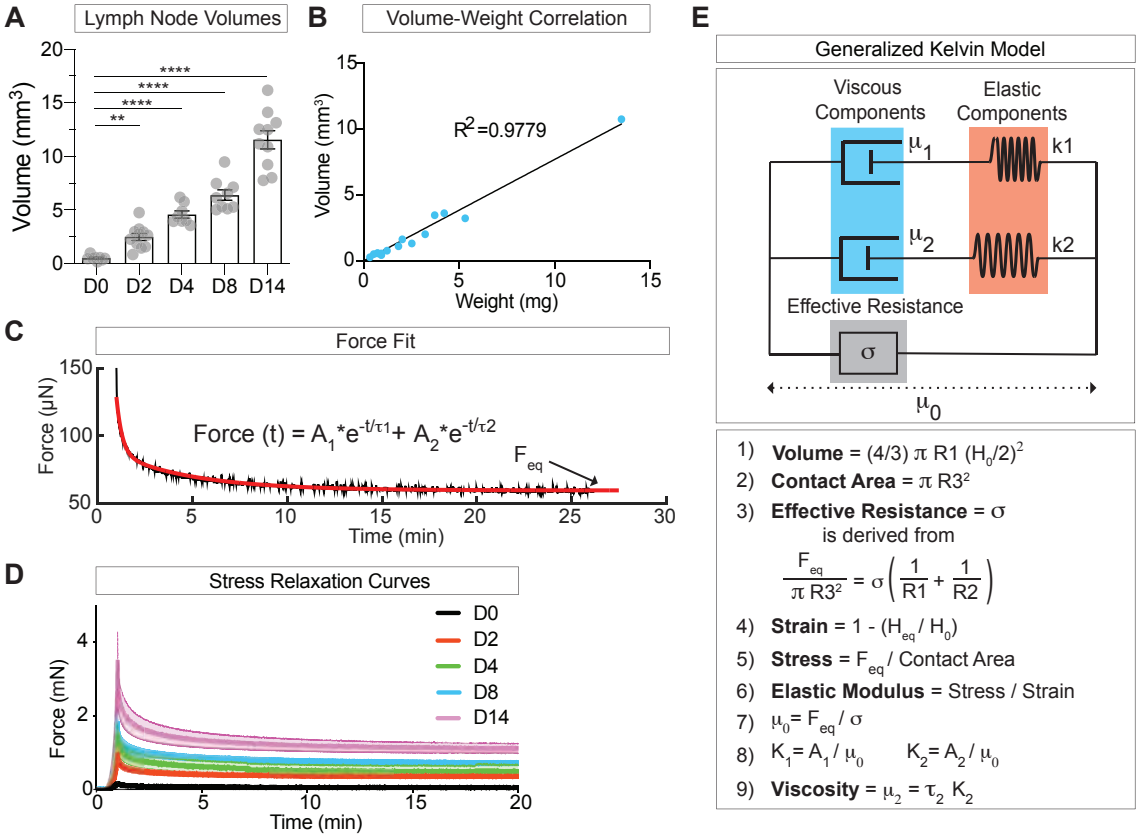

1) **Volume** = $(4/3)\,\pi\, R1\,(H_0/2)^2$
2) **Contact Area** = $\pi\, R3^2$
3) **Effective Resistance** = σ is derived from

$$\frac{F_{eq}}{\pi\, R3^2} = \sigma\left(\frac{1}{R1} + \frac{1}{R2}\right)$$

4) **Strain** = $1 - (H_{eq} / H_0)$
5) **Stress** = F_{eq} / Contact Area
6) **Elastic Modulus** = Stress / Strain
7) $\mu_0 = F_{eq} / \sigma$
8) $K_1 = A_1 / \mu_0$ $\quad K_2 = A_2 / \mu_0$
9) **Viscosity** = $\mu_2 = \tau_2\, K_2$

F

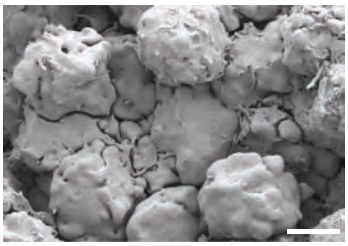

Supplementary Figure 2

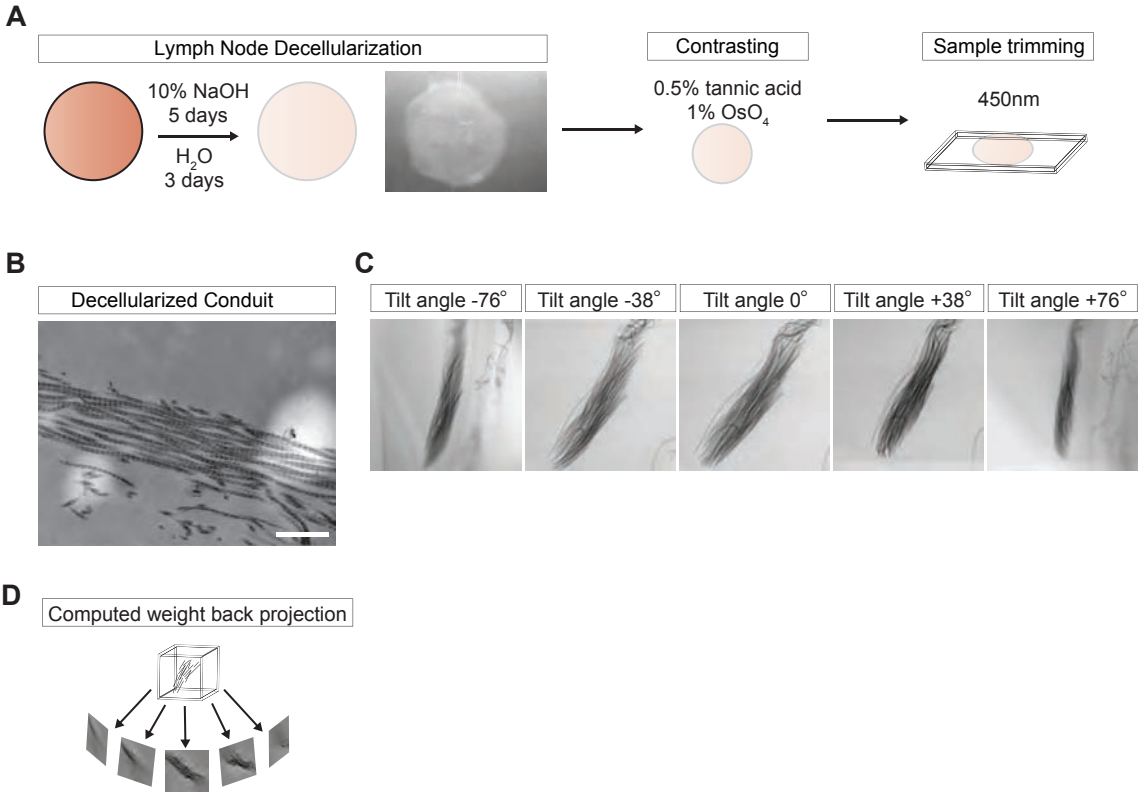

Supplementary Figure 3

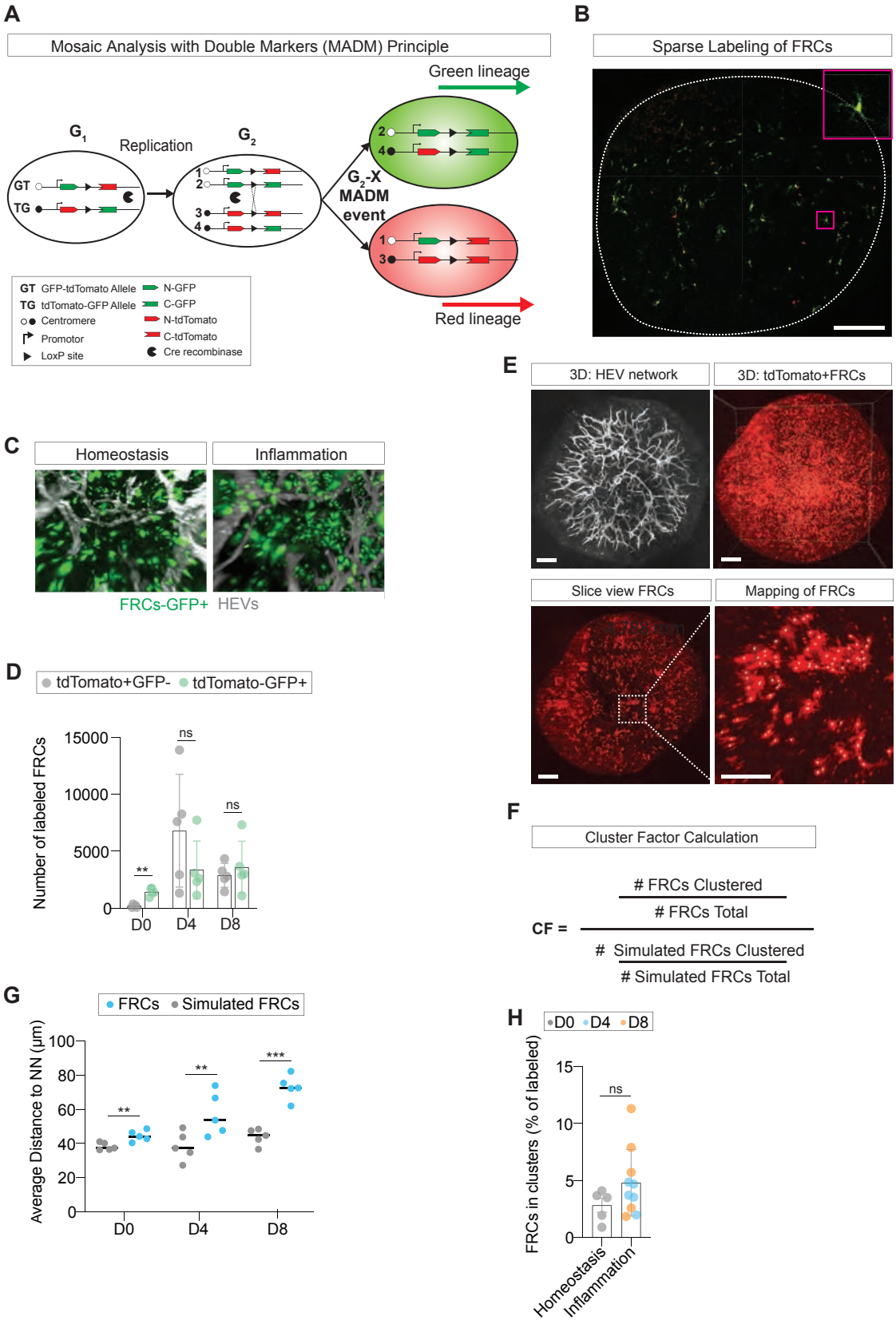

Supplementary Figure 4

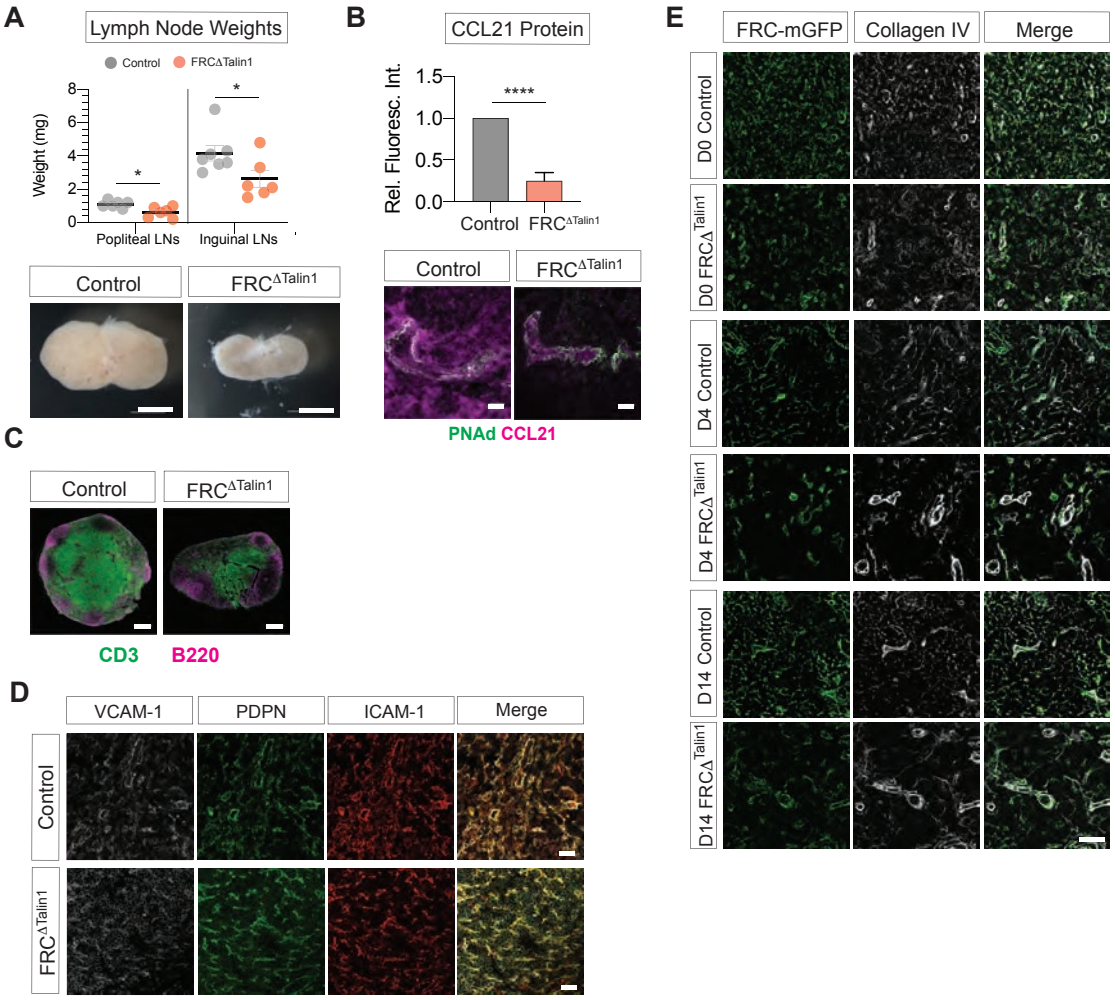
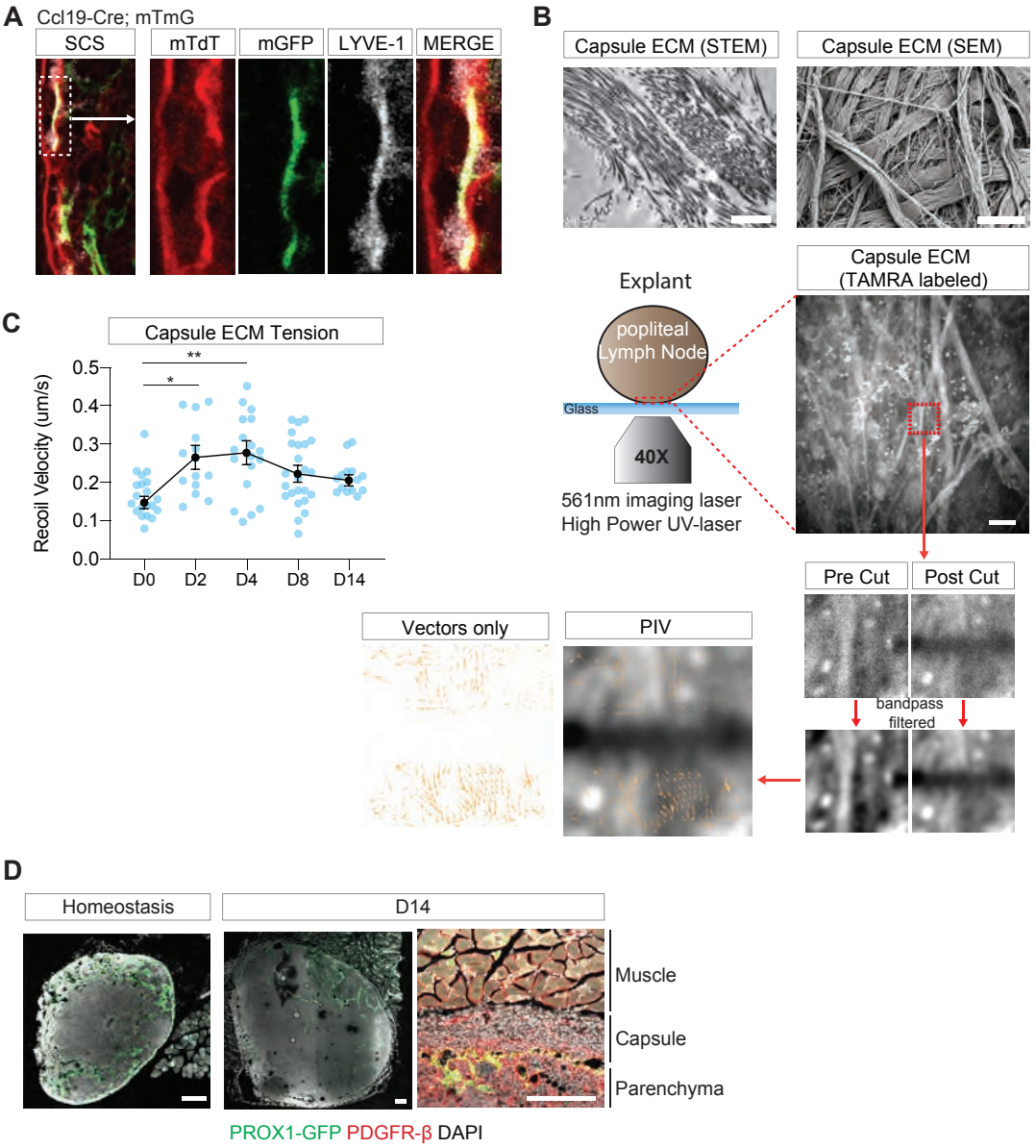
Supplementary Figure 5